Effects of individual base-pairs on *in vivo* target search and destruction kinetics of small RNA

Anustup Poddar[1], Muhammad S. Azam[2,6], Tunc Kayikcioglu[1], Maksym Bobrovskyy[2,7], Jichuan Zhang[1], Xiangqian Ma[2], Piyush Labhsetwar[3,8], Jingyi Fei[4], Digvijay Singh[1,9], Zaida Luthey-Schulten[3], Carin K. Vanderpool[2,*] and Taekjip Ha[1,5,*]

[1]Department of Biophysics and Biophysical Chemistry, Johns Hopkins University School of Medicine, Baltimore, Maryland 21205

[2]Department of Microbiology, University of Illinois at Urbana-Champaign, Urbana, Illinois 61801

[3]Department of Chemistry, University of Illinois at Urbana-Champaign, Urbana, Illinois 61801

[4]Department of Biochemistry and Molecular Biology, University of Chicago, Chicago, Illinois 60637

[5]Howard Hughes Medical Institute, Baltimore, Maryland 21205

[6]Present Address: Department of Biochemistry and Molecular Biology, University of Chicago, Chicago, Illinois 60637

[7]Present Address: Department of Microbiology, University of Chicago, Chicago, Illinois 60637

[8]Present Address: The Land Institute, Salina, Kansas 67401

[9]Present Address: Division of Biological Sciences, University of California, San Diego, San Diego, California 92093

* Corresponding authors

Taekjip Ha, Ph.D. (tjha@jhu.edu)

Carin K. Vanderpool, Ph.D. (cvanderp@illinois.edu)

Abstract

Base-pairing interactions mediate intermolecular target recognition in many biological systems and applications, including DNA repair, CRISPR, microRNA, small RNA (sRNA) and antisense oligo therapies. Even a single base-pair mismatch can cause a substantial difference in biological activity but presently we do not yet know how the target search kinetics *in vivo* are influenced by single nucleotide level changes. Here, we used high-throughput sequencing to identify functionally relevant single point mutants of the bacterial sRNA, SgrS, and quantitative super-resolution microscopy to probe the mutational impact on the regulation of its primary target, *ptsG* mRNA. Our super-resolution imaging and analysis platform allowed us to further dissect mutational effects on SgrS lifetimes, and even subtle changes in the *in vivo* rates of target association, k_{on}, and dissociation, k_{off}. Mutations that disrupt binding of a chaperone protein, Hfq, and are distal to the mRNA annealing region still decreased k_{on} and increased k_{off}, providing an *in vivo* demonstration that Hfq directly facilitates sRNA-mRNA annealing. Single base-pair mismatches in the annealing region reduced k_{on} by 24-31% and increased k_{off} by 14-25%, extending the time it takes to find and destroy the target mRNA by about a third, depending on whether an AU or GC base-pair is disrupted. The effects of disrupting contiguous base-pairing are much more modest than that expected from thermodynamics, suggesting that Hfq also buffers base-pair disruptions.

Introduction

Myriad biological systems use base-pairing interactions for target recognition where proteins mediate base-pairing interactions between two physically separated strands. Such base-pairing-mediated targeting is found in a wide range of processes including DNA repair[1], noncoding RNA-based gene regulation[2,3], bacterial immunity using CRISPR[4], and therapies using anti-sense oligonucleotides[5]. They all rely on base-pairing interactions above a threshold for specificity. How do they achieve both accuracy and speed to sample through thousands of potential targets and rapidly reject non-targets? Recent advances in single-molecule imaging technologies made it possible to explore the kinetic parameters of target recognition and non-target rejection *in vitro*[6–12], and in a limited number of cases, inside living cells[13]. However, we do not yet know the impact of single nucleotide changes in *in vivo* target search kinetics, even though such minute changes can have large functional consequences. Our goal here is to quantify the mutational impact on base-pairing-mediated target search kinetics *in vivo*. We used bacterial gene regulation by small RNA (sRNA) as a model system.

Among the many examples of non-coding RNA-based gene regulation are microRNAs and long non-coding RNAs in eukaryotes and sRNAs in bacteria and archaea[14,3,15]. Often, bacterial sRNAs regulate gene expression at a post-transcriptional level during stress, for example, in iron limitation stress[16], osmotic and acid stress[17], and oxidative stress[18]. Our work here studied the sRNA SgrS, which is produced in response to glucose-phosphate stress.[19]

A disparity between sugar uptake and its metabolism gives rise to stress; a faster uptake leads to an accumulation of glucose-6-phosphate and activation of SgrR, a transcription factor. This stimulates the *sgrS* gene to transcribe SgrS, which reduces sugar transport, promotes efflux and reroutes cellular metabolism[20–22]. Sugar stress conditions are provoked in most studies by

66 subjecting cells to α-methylglucoside (αMG), a sugar analogue that gets phosphorylated during
67 import to form αMG-6-phosphate, which cannot be further processed metabolically. *E. coli*
68 SgrS, a 227-nt sRNA, binds reversibly and dynamically to its primary target, *ptsG* mRNA[23],
69 which codes for the EIICB domain of the glucose phosphotransferase system. Binding between
70 the RNAs, aided by a hexameric RNA chaperone protein Hfq, blocks the *ptsG* ribosome binding
71 site, thereby inhibiting translation of new glucose transporters (Fig. 1a). This sRNA-mRNA
72 complex also gets degraded by endoribonuclease RNase E, thus reducing the cellular
73 concentration of *ptsG* mRNA. Hfq is important for the stability of sRNAs in general and *in vitro*
74 studies have shown that Hfq increases the rate of annealing between sRNA and its target mRNA
75 sequences[24–26]. Whether Hfq also directly facilitates annealing between sRNA and mRNA *in*
76 *vivo* is unknown for any sRNA because it has not been possible to separate the effects of Hfq on
77 sRNA stability and sRNA-mRNA annealing.

78 SgrS contains a 3´ Hfq-binding region predicted to contain two stem-loops, the small stem-loop
79 and the terminator stem-loop that is larger, followed by a U-rich tail (Fig. 1b)[27,28]. An optimal
80 length of U-rich tail, with seven nucleotides or more[27,29], is required for the formation of
81 functional sRNAs and for efficient Hfq binding, and Hfq binding to the two stem-loops is critical
82 for target regulation[27,28,30–32].

83 Nucleotides 168-187 of SgrS are partially complementary to the *ptsG* 5´-UTR (Fig. 1c).[20]
84 Nucleotides 168-181, if presented as a 14 nt long oligonucleotide alone, are sufficient for full
85 repression of *ptsG* translation *in vitro* and *in vivo*[33]. Among these, G176 and G178 have been
86 shown to be most important for the annealing between SgrS and *ptsG* mRNA[24].

87 Previously, we developed a two-color 3D super-resolution imaging and modeling platform to
88 determine *in vivo* target search kinetics for wild-type SgrS regulation of *ptsG*[34]. The bimolecular
89 association rate constant k_{on} between the RNAs was $2x10^5$ $M^{-1}s^{-1}$, which is within the wide range
90 of reported Hfq-mediated sRNA and target mRNA association rates *in vitro* despite the crowded
91 cellular environment and large excess of non–target RNA molecules. The dissociation rate
92 constant k_{off} was 0.2 s^{-1}; 10 to 100-fold larger than *in vitro* estimates of other sRNA-mRNA
93 pairs[32,35,36]. Its non-zero value showed that even for the correct target, binding is reversible. The
94 large dissociation constant K_D (=k_{off}/k_{on}) of ~1 μM explained why more than a hundred SgrS
95 molecules are needed for rapid *ptsG* mRNA regulation. The rate constant for co-degradation, k_{cat},
96 was surprisingly high, 0.4 s^{-1}, suggesting that RNA degradation machineries accompany the
97 target search complex formed between SgrS and Hfq so that as soon as RNAs bind each other,
98 RNAs can be degraded without waiting for the arrival of downstream degradation machineries.
99 Here, by expanding the scale of this quantitative imaging-based investigation by an order of
100 magnitude to include 10 SgrS mutants, we aimed to determine how k_{on}, k_{off} and k_{cat} are affected
101 by single nucleotide changes.

102 We formulated a pipeline of experiments to identify and examine the key regions in SgrS
103 responsible for the annealing and regulation of *ptsG.* We used Sort-Seq, a high-throughput
104 method that can estimate the impact of different mutations on the overall activity of the
105 fluorescence reporter system chosen[37–39]. From the Sort-Seq results, we identified the regions in
106 the SgrS sequence important for the overall regulation and chose nine single nucleotide
107 substitution mutants. *E. coli* strains containing these mutations or one double substitution
108 mutation in their endogenous chromosomal copy were constructed and studied using single-
109 molecule fluorescence *in situ* hybridization (smFISH) followed by 2-color 3D super-resolution

110 imaging and modeling to determine k_{on}, k_{off} and k_{cat}. Our results show that the two stem-loops at
111 the 3´ end of SgrS play important roles in the activity of the sRNA. We also provide *in vivo*
112 evidence that Hfq directly facilitates SgrS-*ptsG* mRNA base-pairing. Importantly, we were able
113 to unambiguously ascribe relative contributions of single base-pairs to sRNA lifetimes and target
114 search kinetics, allowing us to quantify by how much the rates of mRNA binding and rejection
115 are influenced by eliminating a single base-pair between them.

116

117 **Results**

118 **Sort-Seq reveals SgrS nucleotides important for target regulation**

119 We employed a high-throughput Sort-Seq approach to identify SgrS regions important for *ptsG*
120 regulation. We created a low copy number reporter plasmid containing a partial *ptsG* sequence
121 (105 nt 5´- UTR along with the first 30 nt coding sequence of *ptsG* mRNA) and superfolder
122 GFP-coding sequence (*ptsG-sf*GFP)[40] (Supplementary Fig. 1) and transformed it into *E. coli*
123 strain MB1 (Δ*ptsG*, Δ*sgrS*, *lacI*^{q}, *tetR*). The *sgrS* mutation library was constructed by random
124 mutagenesis PCR of a plasmid[40] containing the *sgrS* sequence (Supplementary Fig. 1) and was
125 then transformed into the MB1 strain containing the reporter plasmid (Fig. 2a). The expression of
126 *ptsG-sf*GFP and *sgrS* were under the control of $P_{Llac-O1}$ and $P_{Ltet-O1}$, respectively, and were
127 induced by Isopropyl β-D-1-thiogalactopyranoside (IPTG) and anhydrotetracycline (aTc). Upon
128 induction by IPTG, cells containing the target reporter (*ptsG-sf*GFP) alone showed bright
129 fluorescence, while those co-transformed with the plasmid containing wild-type *sgrS* showed
130 weak GFP fluorescence in the presence of both IPTG and aTc in single-cell imaging
131 (Supplementary Fig. 2) and flow cytometry analysis (Fig. 2b), indicating an effective repression

132 of the reporter. Cells co-transformed with the *sgrS* mutant library showed a broad distribution of
133 GFP fluorescence indicating highly variable levels of regulation by mutants (Fig. 2b). Based on
134 the flow cytometry results, the cells were collected in five intensity bins, and the plasmids were
135 extracted from the cells. For each bin, the mutated *sgrS* sequence from position 149 to 227 was
136 amplified by PCR and sequenced. Sequencing was limited to this region because the 5´ region,
137 up to nucleotide 153 and coding for the 43 amino acid peptide SgrT, is not involved in base-
138 pairing-dependent mRNA regulation[41,42].

139 Using the relative abundance of sequences in each bin and the GFP fluorescence levels from the
140 flow cytometry analysis, we calculated, for each single point mutation, the average fluorescence
141 intensity of cells sharing the same mutation as a measure of the regulation defect (Fig. 2d).[39]
142 High average single cell fluorescence would correspond to SgrS mutants that are highly
143 defective in regulation of *ptsG* reporter expression and vice versa. The degree of perturbation to
144 the regulatory capacity is color-coded in the heatmap grid, ranging from the least (blue) through
145 intermediate (white) to the most (red). Nucleotides 149 to 174 showed little to no perturbation of
146 SgrS regulation as shown by the blue squares (Fig. 2d). In contrast, the region where SgrS can
147 base-pair with *ptsG* mRNA (U175 to G186) displayed perturbations across a wide range as
148 shown by the white and red squares in the grid. Specifically, previous studies showed that
149 G176C or G178C eliminates the SgrS's ability to downregulate *ptsG* while C174G and G170C
150 only weakly perturbs SgrS function *in vivo* and *in vitro*[24,31]. The corresponding squares in our
151 heatmap grid (Fig. 2d) show red or dark red for G176C and G178C, and white or light blue for
152 C174G and G170C, validating our Sort-Seq results. We also see that SgrS regulation is
153 hampered if there are mutations in the small stem-loop region (nts 183-196 (Fig 1b)), the
154 terminator stem-loop region (nts 199-219) and the poly-U tail (nts 220-227). The largest effect is

155 seen in the stem region of the terminator stem-loop, C199 to G205 and C213 to G219, where we
156 see the darkest red, highlighting the importance of this stem-loop. These stem-loop regions and
157 the poly-U tail play a role in Hfq binding[27,28], and our Sort-Seq analysis therefore confirms that
158 Hfq interaction is important for SgrS function in the cell.

159 Based on Sort-Seq results, we picked nine single point mutations for further investigation. These
160 include mutations in the target annealing region (A177U, G178A, G178U, U181A), U-rich
161 region upstream of the small stem-loop (U182A), the small stem-loop (G184A), the terminator
162 stem-loop (G215A) and the poly-U tail (U224G, U224A).

163

164 **SgrS mutation effects on regulation of *ptsG* reporter**

165 To examine the effect of the selected SgrS mutations on *ptsG* regulation, we monitored the effect
166 of wild-type and seven of the SgrS mutants (plasmid-encoded and expressed from an inducible
167 promoter) on the activity of a chromosomal *ptsG'-'lacZ* translational fusion (Fig. 3a). The wild-
168 type SgrS almost completely eliminated β-galactosidase activity whereas the mutants showed
169 regulation defects of various degrees consistent with the Sort-Seq data. SgrS G215A, which
170 disrupts the terminator stem-loop structure, showed the largest defect. To test if the regulatory
171 defects can be explained by a reduction of SgrS levels, for example, due to shorter cellular
172 lifetimes associated with impaired Hfq binding, we performed Northern blot analysis. We found
173 that SgrS abundance is not affected for four of the mutants (A177U, G178U, G178A and
174 G184A) and is reduced by 40-50% for mutations in the terminator stem-loop or poly-U tail
175 (G215A, U224G and U224A) (Fig. 3c). Interestingly, the latter three mutants showed large
176 increases in readthrough transcription, suggesting that transcription termination is defective (Fig.

177 3d). These observations are consistent with a previous study which showed that SgrS molecules
178 with an extended 3′ region do not interact with Hfq[43]. Overall, single point mutations outside the
179 large terminator stem-loop and poly-U tail have minimal impact on SgrS abundance and their
180 regulatory defects cannot be explained by SgrS abundance changes.

181

182 **Super-resolution imaging of specific chromosomal SgrS mutants**

183 A set of 9 single point mutants of SgrS were chosen for further analysis using quantitative
184 imaging (A177U, G178A, G178U, G184A, U181A, U182A, G215A, U224A, U224G). To avoid
185 potential complications arising from SgrS overexpression, we created these mutations in the
186 endogenous chromosomal copy of SgrS. A177, G178 and U181 are in the seed (target base-
187 pairing) region, G184 is in the small stem-loop region. U181 and U182 are in the U-rich region
188 upstream of the small stem-loop, previously shown to bind Hfq[27]. We also constructed a double-
189 mutant G184A-C195U which restores the small stem-loop structure. G215 is in the terminator
190 stem-loop region and U224 is in the poly-U tail, both of which provide major binding sites for
191 Hfq. These mutant alleles in the background of strains with wild-type RNase E or a C-terminally
192 truncated RNase E were grown, and glucose-phosphate stress was induced using αMG for a
193 varied amount of time before cell fixation and permeabilization. We performed two-color 3D
194 super-resolution imaging of the SgrS sRNAs labeled with up to 9 FISH probes conjugated to
195 Alexa Fluor 647 and the *ptsG* mRNAs labeled with up to 28 FISH probes conjugated to CF568.
196 Δ*sgrS* and Δ*ptsG* strains were also examined to correct for the background arising from
197 nonspecific binding of FISH probes. The wild-type strain showed an increase in SgrS copy
198 number over time after sugar stress induction (Fig. 4, Supplementary Fig. 3). At the same time,
199 the copy number of *ptsG* mRNA showed a decrease (Fig. 4, Supplementary Fig. 3). We used a

density-based clustering algorithm[34] to determine the copy numbers of RNAs along with the copy number of SgrS-*ptsG* mRNA complexes. Super-resolution imaging was especially important for quantifying sRNA-mRNA complexes because at conventional microscopy resolution there was too much false co-localization between sRNA and mRNA.

The accumulation of the mutant SgrS sRNAs was lower than for wild-type SgrS with an accompanying impairment in *ptsG* mRNA degradation for all single point mutants examined, showing that their regulatory functions are perturbed (Fig. 4, Supplementary Fig. 4-9, 11-13). The single cell distribution of RNA copy numbers also showed a decreased accumulation of SgrS, with the histogram peaking at lower copy numbers 20 min after αMG induction, and the histograms for *ptsG* mRNA peaked at higher copy numbers per cell compared to the wild-type (Fig. 5b, d, h, Supplementary Fig. 52). The lowest accumulation of SgrS was seen for G184A and G215A, and they also showed the most impaired mRNA degradation (Fig. 4, 5a, c, g, Supplementary Fig. 9, 11). These two mutations occur in two separate stem-loop regions, both of which participate in Hfq binding.[27,28] The double mutant, G184A-C195U, which restores base-pairing in the small stem-loop via a compensatory mutation, eliminated the negative impact of G184A as seen by recovery of SgrS accumulation and regulation of *ptsG* mRNA (Fig. 4, 5e, f, Supplementary Fig. 10). This suggests that the disruption of the stem-loop structure, not of G184 basepairing with *ptsG* mRNA, is primarily responsible for regulatory defects of G184A.

These imaging data by themselves cannot tell us whether regulatory defects are due to changes in target binding kinetics or due to changes in the SgrS stability. Therefore, we next determined the lifetimes of wild-type and mutant SgrS molecules.

222 **Intrinsic lifetimes of SgrS mutants**

223 In order to calculate the target-independent lifetime of SgrS, we induced SgrS expression using
224 αMG and then added rifampicin to stop transcription globally. RT-qPCR was performed vs time
225 after rifampicin treatment to quantify the SgrS level. The wild-type SgrS showed minimal
226 intrinsic degradation over a period of 2 hours after the addition of rifampicin but it showed rapid
227 degradation in the presence of ongoing transcription (10.4 ± 0.7 min), suggesting that SgrS
228 degradation is normally dominated by co-degradation with its various target mRNAs (Fig.
229 Supplementary Fig. 25). The intrinsic degradation was also minimal for SgrS A177U mutant
230 (Supplementary Fig. 25), suggesting that in the absence of co-degradation, a mutation in the
231 target-annealing region does not destabilize SgrS. In contrast, intrinsic degradation of G184A
232 was rapid (lifetime of 6.3 min) and so was the intrinsic degradation of wild-type SgrS in Δ*hfq*
233 strain (lifetime of 5.1 min) (Supplementary Fig. 25), indicating that Hfq is required for the target-
234 independent stability of SgrS and the small stem-loop is important for Hfq binding.

235

236 **Lifetime of SgrS mutants**

237 In order to determine the effective lifetime of SgrS mutants, which includes the contributions
238 from intrinsic degradation and co-degradation with target mRNA, the strains carrying
239 chromosomal mutations were treated with αMG for 10 minutes before rinsing it away. SgrS
240 decay over time was then monitored through imaging of fixed cells. The wild-type SgrS showed
241 a degradation rate of 0.0016 ± 0.0001 s^{-1} (lifetime of 10.4 ± 0.7 min) and all of the mutants
242 showed higher rates, the highest being for G184A with 0.0046 ± 0.0003 s^{-1} (lifetime of 3.6 ± 0.2
243 min), followed by G215A with 0.00345 ± 0.0003 s^{-1} (lifetime of 4.8 ± 0.4 min) (Fig. 6a,

244 Supplementary Fig. 26-32, 34-36). Because G184A and G215A disrupt the small and terminator
245 stem-loop regions, respectively, our data suggest that both stem-loop regions are important for
246 SgrS stability *in vivo*. G184A-C195U recovered the stability of SgrS to the wild-type level with
247 an identical degradation rate within error (Fig. 6a, Supplementary Fig. 33). Rifampicin-chase
248 experiments did not show any difference in the lifetime of *ptsG* mRNA between all mutant
249 strains (Supplementary Fig. 26-37), showing that the mutations in SgrS have no effect on *ptsG*
250 mRNA stability when SgrS is not induced.

251 The degradation rate of SgrS in Δ*hfq* strains was much higher, about $0.022 \pm 0.004\ s^{-1}$ (lifetime
252 of 0.76 ± 0.14 min), for wild-type and all SgrS mutants (Fig. 6a, Supplementary Fig. 38-40) [23].
253 This 14-fold increase in degradation rate for sRNAs in Δ*hfq* strains confirms that Hfq is
254 indispensable for the stability of SgrS[27,44]. Because none of the SgrS mutants in the hfq^+ cells
255 showed degradation rates as high as in Δ*hfq* strains, these SgrS mutations are only partially
256 deleterious to the interactions with Hfq.

257 Mutations in the base-pairing regions (A177U, G178U and G178A) reduced the lifetime of SgrS
258 in the imaging-based experiment even though they are not expected to alter Hfq binding.
259 Because our Northern blot analysis of overexpressed SgrS showed that these mutations do not
260 change SgrS abundance, the intrinsic degradation is unlikely to be affected by the mutations.
261 Instead, we attribute the discrepancy to mutation-induced alterations in co-degradation of SgrS
262 with other SgrS target mRNAs.

263

264 **Target search and destruction kinetics of SgrS mutants**

265 Once we obtained the average copy numbers of SgrS, *ptsG* mRNA and the SgrS-*ptsG* complex
266 per cell as a function of time after SgrS induction for the full length RNase E and RNase E
267 mutant cases (Supplementary Fig. 14-24), we used a previously developed deterministic kinetic
268 model to describe the SgrS-*ptsG* regulation kinetics (Fig. 1a)[34]. We used the experimentally-
269 determined degradation rate for *ptsG* mRNA, β_p, to calculate the *ptsG* transcription rate α_p using
270 $\alpha_p = \beta_p \times [p]_0$, where $[p]_0$ is the steady state copy number of *ptsG* mRNA at t=0. By globally
271 fitting the six time courses of the three RNA species with or without RNase E mutation that
272 inhibits co-degradation, we obtained k_{on}, k_{off} and k_{cat} for the wild-type and mutant SgrS.

273 k_{on} for the wild-type strain was (1.9 ± 0.2) x 10^5 M^{-1}-s^{-1} and k_{off} was 0.22 ± 0.02 s^{-1} giving a
274 K_D of 1.16 ± 0.14 μM, comparable to the previously published results (Fig. 6b-d)[34]. k_{on} was
275 lower for all single point mutants compared to the wild-type and the reduction ranged from 24%
276 for A177U to 53% for G184A. k_{off} was higher for all the mutants and the increase ranged from
277 14% for A177U to 33% for G184A giving a dissociation constant, K_D of 1.67 ± 0.13 μM and
278 3.08 ± 0.33 μM, respectively (Fig. 6b-d). Rate of transcription of SgrS and k_{cat} were not affected
279 by the mutations within error (Supplementary Fig. 42-43). To test the possibility that the
280 apparent changes in k_{on} and k_{off} are due to fitting errors and that the regulatory deficiencies can
281 be explained solely by reduction in SgrS lifetimes, we repeated the global fitting procedure while
282 keeping the k_{on} and k_{off} values fixed at the wild-type values. The fits were considerably worse,
283 and were especially poor for copy number curves of *ptsG* mRNA and SgrS/mRNA complex
284 (Supplementary Fig. 44-51). Therefore, our procedure of obtaining the mutation effects on k_{on}
285 and k_{off} is robust.

286 When we restored the base-pairing in the small stem-loop by adding a compensatory mutation to
287 G184A, the mutant that showed the largest changes to k_{on} and k_{off} (G184A-C195U), k_{on} and k_{off}
288 returned to the wild-type values within error (Fig. 6c-d). Nucleotides 168-187 in SgrS were
289 originally proposed to participate in base-pairing with the *ptsG* mRNA[20] but a subsequent study
290 showed that only nucleotides 168-181 are required for basepairing[33]. Here we found that binding
291 kinetics is similar between the wild-type and G184C-C195U, strongly suggesting that a mutation
292 at G184 primarily acts through disruption of the small stem-loop structure, thereby affecting Hfq
293 binding, instead of through direct disruption of base-pairing of G184 with the target strand. Even
294 though our data suggest that G184 is not involved with SgrS-*ptsG* mRNA base-pairing, its
295 mutation negatively affected annealing kinetics, decreasing k_{on} and increasing k_{off}. Therefore, our
296 results support the dual roles of Hfq: first to increase sRNA stability (Fig. 6a) and second to
297 directly facilitate SgrS-*ptsG* binding.

298 The A to U mutation at position 177 removes an AU base-pair, breaking 8 base-pairs, the longest
299 stretch of contiguous base-pairing between SgrS and *ptsG* mRNA into segments of 4 and 3 base-
300 pairs. This disruption gives a reduction in association rate of 24% and an increase in dissociation
301 rate by 14%. The two mutations at position 178 eliminate a GC base-pair and breaking the same
302 8 base-pairs into segments of 3 and 4 base-pairs. G178A and G178U mutants gave a reduction of
303 association rate by 31-32% and an increase of dissociation rate by 23-25%. The larger effects of
304 G178 mutations compared to A177U are likely due to the loss of GC over AU base-pair.
305 Consistent with this suggestion, a mutation at U181, losing an AU base-pair, decreased the
306 association rate by 26% and increased the dissociation rate by 18%, very similar to A177U
307 values.

308 The G215A mutation in the terminator stem-loop and the mutations U224A and U224G in the
309 poly-U tail showed k_{on} decreases and k_{off} increases even though they should not change
310 complementarity between SgrS and *ptsG* mRNA. The substantial effects on binding kinetics
311 must therefore be due to defects in Hfq's ability to facilitate the annealing reaction, further
312 providing *in vivo* evidence of direct facilitation of base-pairing between sRNA and mRNA by
313 Hfq.

314

315 **Difference in regulation outcome between imaging and Sort-Seq experiments**

316 To examine if the regulation outcomes for SgrS mutants is consistent between our quantitative
317 imaging experiments and Sort-Seq analysis, we used the fractional decrease of *ptsG* mRNA over
318 the first 20 min after sugar stress induction as a measure of the SgrS regulation of *ptsG* mRNA
319 target in imaging-based analysis. (Fig. 6e-g). Plotting these values vs the inferred GFP signals
320 obtained from the Sort-Seq experiments, we observed a relatively weak correlation (Pearson's R
321 = 0.71), suggesting that the translation reporter-based Sort-Seq method is not able to fully
322 capture the regulation defects of SgrS mutations. For example, G178A which had a large
323 deficiency in regulation in imaging experiments showed almost the wild-type level regulation in
324 Sort-Seq. A large defect in regulation was shown in previous studies where nucleotide 178 was
325 mutated and our imaging-based approach is in accordance to this finding[24]. SgrS overexpression
326 in Sort-Seq may have overcome the negative effect of mutations through mass action when the
327 defect is primarily in binding kinetics. For the G215A, U224A and U224G mutant strains,
328 however, Sort-Seq showed large regulatory deficiencies, suggesting that their defects cannot be
329 overcome by overexpression. There are several possible explanations. First, because Sort-Seq
330 relies on the translational output, mutations that disrupt translational inhibition but not RNA co-

331 degradation may not be scored well in imaging-based experiments. However, *in vitro* translation
332 experiments showed that mutation of G178 to C eliminates translation inhibition by SgrS[33],
333 making it unlikely that defects in RNA-RNA annealing do not affect translational repression.
334 Second, even when these mutants can bind Hfq, the complex may be defective in mediating
335 RNA annealing. Third, these mutations also interfere with proper termination as shown by
336 readthrough transcripts (Fig. 3). It was shown previously that the readthrough products of SgrS
337 transcription do not bind Hfq *in vivo* and *in vitro*[43]. Weakening of the terminator stem-loop or
338 reduction of the slippery Us must be causing transcription readthroughs that produce regulation-
339 defective products, and much of the effect of G215A, U224A or U224G may be due to improper
340 termination. It has also been shown that readthrough transcription of SgrS is suppressed under
341 stress conditions, providing an additional layer of regulation[43]. Finally, the incorporation of the
342 GFP in the reporter system may have affected the stability of the mRNA.

343

344 **Discussion**

345 Previous studies have measured the effect of mutations in the regulation of mRNA targets of
346 SgrS[45–47] and have shown the importance of Hfq, sequence complementarity between SgrS and
347 its targets, and RNA secondary structures[27,33,48,49]. Hfq has also been shown to promote structural
348 changes to the RNAs, which in turn helps in the annealing and, consequently, regulation[50–52].
349 Our study provides a quantitative description of the process of target search and off-target
350 rejection by determining the kinetic parameters as a function of single nucleotide changes in
351 functionally important regions. The k_{on} and k_{off} values determined in this study depict the
352 apparent rate constants because we did not explicitly include Hfq binding in our model. k_{on} in

353 particular should have contributions from Hfq binding to SgrS, target search by SgrS/Hfq and
354 subsequent annealing.

355 We used IntaRNA[53–56] to predict the energy of interaction between SgrS and *ptsG* mRNA and
356 found that it changes by ~6.4 kcal/mol for the G178 point mutations whereas the change is only
357 around ~4.3 kcal/mol for A177U. Our study agreed with the ranking because we saw lower rates
358 of association and higher rates of dissociation for G178 than A177U. However, the magnitude of
359 the effect is much more modest compared to a simple prediction based on the energetic penalty.
360 Both mutations introduce a mismatch within eight contiguous base-pairs, incurring large
361 energetic penalties. For example, 6.4 kcal/mol would correspond to a change in the equilibrium
362 binding constant by a factor ~60,000 instead of ~2 we observed. Therefore, Hfq must be
363 buffering the effect of breaking internal base-pairs in short helices. How this is achieved is
364 presently unknown.

365 We found that the rate of co-degradation remains high, ~0.3 s^{-1}, even with SgrS mutations. The
366 co-degradation of the SgrS-*ptsG* complex is brought about by the degradosome, in which RNase
367 E is a key component. Hfq copurifies with RNase E and SgrS[57], and at least one sRNA (MicC)
368 has been shown to mediate the interaction between Hfq and the C-terminal part of RNase E *in*
369 *vitro*[58] and *in vivo*[59]. It has been hypothesized that the sRNA-Hfq-RNase E complex forms first
370 and subsequently the complementary mRNA binds to this complex, aided by Hfq, followed by a
371 coupled or sequential degradation of the RNA pair[58]. The changes in k_{on} and k_{off} in our study
372 account for the disruption of the SgrS-*ptsG* mRNA annealing, but once a stable complex with all
373 four components forms, the co-degradation occurs at the same rate irrespective of the SgrS
374 mutations.

375 Because k_{cat} did not change with SgrS mutations, the probability that a single binding event will
376 cause co-degradation of sRNA and mRNA decreases with a mutation-induced increase in k_{off}. On
377 average, the wild-type SgrS would take 1.73 (= $(k_{off}+k_{cat})/k_{cat}$) binding events before co-
378 degradation. This number increases to 1.81 when AU basepairing is disrupted by a mutation and
379 increases further to 1.9 when GC basepairing is disrupted. In addition, the binding rate at the full
380 SgrS accumulation condition, 100-200 copies per cell, would correspond to 0.48 μM (assuming
381 0.7 μm^3 per cell), and the wild-type SgrS would take about 11 s to bind *ptsG* mRNA. If a mutant
382 SgrS were present at the same concentration, it would take ~13.6 s and ~14.4 s to bind for
383 disrupting a single AU and GC base-pair, respectively. The overall time it takes to degrade the
384 target would increase from 19 s to 24.6 s and 27.4 s for disrupting an AU and GC base-pair,
385 respectively. Although we examined only the effect of SgrS mutation in this study, if we assume
386 that a mutation in the target mRNA breaking a single base-pair has a similar impact, we can
387 conclude that target search and destruction will take 29-44 % longer for nearly cognate off-target
388 RNA containing a single base-pair mismatch.

389 The poly-U sequence at the 3' end of sRNAs is an important Hfq binding module[29,43] and binds
390 to the proximal face of the ring-shaped Hfq hexamer[29,50] . Because Hfq forms a stable 1:1
391 complex with SgrS[27], a single Hfq hexamer must bind the poly-U tail, both of the stem-loops,
392 and the UA-rich region upstream of the small stem-loop simultaneously. How this is achieved
393 requires further structural studies, but the UA-rich region has been found in other sRNAs and has
394 been proposed to bind the rim of the Hfq hexamer[27,51,60–62]. The binding of Hfq with target
395 mRNAs, however, has been studied extensively and it is known that Hfq brings about a
396 distortion in the mRNA structure, promoting the base-pairing between the RNAs[63,64]. In this
397 study we showed that the U224 mutations in the poly-U tail caused the rate of association of the

398 RNAs to decrease and the rate of dissociation to increase. Because U224 is distant from the
399 mRNA annealing region of SgrS, our data showed that Hfq directly facilitates RNA-RNA
400 annealing *in vivo*. The same effect was observed from other mutants that disrupt Hfq binding
401 without changing the mRNA annealing region of SgrS, and collectively our work presents the
402 first *in vivo* evidence that Hfq directly facilitates target binding. It should be emphasized that a
403 careful accounting of SgrS mutations' effects on SgrS lifetimes was necessary to reach this
404 conclusion. Microscopic mechanisms for Hfq's role in sRNA-mRNA annealing are still a subject
405 of active research[60,65,66], and may be investigated in the future using our analysis platform.

406

407 **Materials and Methods**

408 **Construction of plasmids for Sort-Seq studies**

409 A *ptsG-sf*GFP reporter system was constructed, containing 105 nt 5′ UTR and 30 nt coding
410 sequence of *ptsG* mRNA, which coded for the first 10 amino acids of PtsG protein, and this was
411 fused by a 42 nt linker sequence and the superfolder GFP coding sequence. The reporter system
412 was subcloned from the pZEMB8 plasmid. A plasmid, pAS06 was constructed by inserting this
413 reporter sequence into the low copy plasmid pAS05 between the XhoI and XbaI restriction sites
414 and the expression of the reporter system was under the control of $P_{Llac\text{-}O1}$.

415 The SgrS sRNA sequence was inserted in between the NdeI and BamHI restriction sites of the
416 medium copy plasmid pZAMB1 and its expression was under the control of $P_{Ltet\text{-}O1}$. The sgrS
417 mutation library was prepared by using the plasmid pZAMB1 as a template for mutagenesis PCR
418 and also as a vector to insert the *sgrS* mutation sequence.

419 **Cell culture and induction for Sort-Seq studies**

420 The *E. coli* MB1 strain (Δ*ptsG*, Δ*sgrS*, *lacI*^{q}, *tetR*) was transformed with plasmids (pAS06 for
421 *ptsG-sf*GFP and pZAMB1 for *sgrS* or the SgrS mutation library) and grown at 37 ºC in LB Broth
422 Miller (EMD) overnight with the respective antibiotics (100 µg/ml ampicillin (Gold
423 Biotechnology, Inc.)) for pAS06 plasmid and 30 µg/ml chloramphenicol (Sigma-Aldrich) for
424 pZAMB1 plasmid and the *sgrS* mutation library). The following day, the cell culture was diluted
425 200-fold into fresh LB Broth with respective antibiotics and were grown until OD_{600} reached 0.1-
426 0.2 as measured using an Educational Spectrophotometer (Fisher Scientific Education). The
427 culture was diluted again to an OD_{600} of 0.001 and supplemented with 1 mM IPTG (Sigma-
428 Aldrich) to induce the expression of PtsG-*sf*GFP and 50 ng/ml aTc to induce the expression of
429 SgrS or the SgrS mutation library. The *E. coli* cells were collected and treated further for the next
430 set of experiments.

431 **SgrS sRNA mutagenesis experiment**

432 Agilent Genemorph II Random Mutagenesis Kit (Agilent Technologies) was used to perform
433 mutagenesis PCR on SgrS using the protocol adapted from previously published work from
434 Levine's lab[39]. 1 ng of pZAMB1 plasmid, with the *sgrS* sequence, was used to conduct
435 mutagenesis PCR for 15 cycles. The yields of the individual mutants were increased by
436 amplifying the product using Phusion® High-Fidelity DNA Polymerase (New England Biolabs)
437 and purified using QIAquick Spin Columns (Qiagen) . The PCR products were then digested
438 with NdeI (New England Biolabs) and BamHI (New England Biolabs) and purified by QIAquick
439 Spin Columns (Qiagen). The pZAMB1 vector was also prepared by digestion with NdeI and
440 BamHI followed by purification using QIAquick Spin Columns (Qiagen). The vector and the
441 PCR insert were used to prepare 4 ligation reactions by mixing with T4 Ligase (New England
442 Biolabs).

443 The products from all the reactions were combined and purified using QIAquick Spin Columns
444 (Qiagen) into water. 5 µl of the purified ligation product was then transformed into MB1 strain,
445 which was pre-transformed with pAS06 plasmid expressing *ptsG-sf*GFP. These transformed cells
446 were then recovered and diluted into LB Broth supplemented with 100 µg/ml ampicillin and 30
447 µg/ml chloramphenicol and grown overnight at 37 ºC. The following day, the culture was
448 centrifuged, aliquoted as frozen stocks and used for imaging and flow cytometry experiments.

449 **Epifluorescence Imaging**

450 1 ml culture of the *E. coli* strain to be imaged was grown from an overnight culture till OD_{600} =
451 0.1-0.2. It was then chilled on ice followed by centrifugation at 6000 g, 4 ºC for 1 minute to form
452 a cell pellet. Then they were washed with ice-cold 1X PBS twice and resuspended in 100 µl 1X
453 PBS.

454 1.5% (w/v) agarose gel was prepared by dissolving agarose in 1X PBS. A few µl cell suspension
455 was sandwiched between a No. 1.5 glass coverslip (VWR) and a thin slab of the agarose gel. The
456 sample was then imaged.

457 The epifluorescence images were acquired by a Nikon Ti Eclipse microscope (Nikon
458 Instruments, Inc.) using an oil immersion objective (1.46 NA, 100X) which spans an area of
459 around 133x133 μm^2 for DIC (no filter, autofluorescence) and fluorescence imaging (Ex 480-
460 500 nm, Em 509-547 nm, exposure time 200 ms). The images were acquired using an EMCCD
461 camera (Andor). They were processed using the NIS-Element AR software (Nikon Instruments,
462 Inc.).

463 **Fluorescence-Activated Cell Sorting**

464 The *E. coli* strain to be sorted was cultured overnight in LB Broth with appropriate antibiotics.
465 The following day, the liquid culture was diluted 200-fold and cultured with antibiotics until
466 OD_{600} = 0.1-0.2. The cells were then diluted to OD_{600} = 0.001 in LB Broth with antibiotics and 1
467 mM IPTG and/or 50 ng/ml aTc were added corresponding to the strain of *E. coli* and the
468 plasmids it is carrying. They were grown till OD_{600} = 0.1-0.2, washed with ice-cold 1X PBS
469 twice and kept on ice before flow cytometry analysis or fluorescence-activated cell sorting. The
470 sorting and analysis were done in a MoFlo XDP Cell Sorter (Beckman Coulter) using a 488nm
471 200mW laser.

472 **Preparation of the sample for sequencing**

473 The cells sorted into the batches were grown in LB Broth supplemented with 30 μg/ml
474 chloramphenicol to saturation. We extracted the plasmids with E.Z.N.A. Plasmid Mini kit
475 (Omega, D6942-02). To generate sequencing amplicons, we followed Illumina 16S sequencing
476 protocol. We used 5 ng of each plasmid elute as PCR template and amplified out the portion of
477 interest using 0.5 μM of primers annealing to the region of the *sgrS* sequence under
478 consideration with Phusion 2X Mastermix (NEB, M0531L). We employed 20 cycles of 10 s at
479 98 ºC denaturation, 20 s at 63 ºC primer annealing, 10 s at 72 ºC elongation phases preceded by
480 additional initial denaturation at 98 ºC for 30 s and followed by 72 ºC final extension for 2 min.
481 To clean up the product, we incubated the PCR product with 20 μl Ampure XP beads (Beckman
482 Coulter, A63880) for 5 min. We retained the bead-bound material after keeping for 2 minutes on
483 a magnetic rack (GE, 1201Q46). We washed the beads twice with 80% ethanol, air-dried for 10
484 min and eluted the material in 53 μl 10 mM Tris pH 8.5 by incubation for 2 min. We collected
485 45-50 μl bead-free liquid 2 min after placing the material on a magnetic rack.

486 **Illumina Next-Gen Sequencing**

487 We performed 8 additional cycles of PCR with Nextera 24-Index kit for indexing before sample
488 pooling (Illumina, FC-121-1011), for which we used 7.5 µl of the above elute as template, 7.5 µl
489 each of the suitable i5 and i7 primers with 38 µl Phusion 2X Mastermix. We followed
490 manufacturer's recommended thermal cycling protocol (95 ºC 3min, 98 ºC 30s, 55 ºC 30s, 72 ºC
491 30s, 72 ºC 5min). We also bead-purified 55 µl of this final product with 56 µl Ampure-XP beads
492 and eluted with 28 µl 10 mM Tris pH 8.5 buffer. We pooled the final products based on their
493 Nanodrop reading at equal molar stoichiometry and diluted the sample down to 4 nM in 10 mM
494 Tris buffer. We alkaline-denatured by mixing 5 µl DNA sample with 0.2 M NaOH and
495 incubating for 5 min at room temperature. We diluted this product down to 20 pM in Hbf buffer.
496 We loaded a final mixture of 465 µl Hbf buffer, 120 µl pooled 20 pM library and 15 µl denatured
497 20 pM PhiX control library (Illumina, FC-110-3001) after a 2 minute heat treatment at 96 ºC
498 followed by a 5 min incubation on ice. We used a 150 cycles MiSeq v3 reagent kit (Illumina,
499 MS-102-3001) to perform a single-end sequencing for 150 cycles. We used the manufacturer's
500 default algorithm for base calling and de-multiplexing of the constituent samples.

501

502 **Intensity Moment Calculation**

503 We parsed the raw .fastq output files via a simple home-made C++ script compiled with GCC v.
504 7.5 and plotted with GNU Octave v. 4.2. The analysis scripts can be accessed via the Gitlab page
505 https://gitlab.com/tuncK/sortseq/-/tree/master and the raw data can be obtained from TH upon
506 request.

507 We only imported the base calls of each read, thus including all sequences regardless of their
508 quality factors. We directly extracted from each read the subsequence excluding the PCR
509 adaptors, i.e. bases 23 to 128. Out of this list of subsequences, we detected ones that are exact
510 duplicates of each other by building a red-black binary search tree. Among all such groups, we
511 only considered SgrS sequence variants that are represented by at least 10 distinct reads in the
512 data. We compared the observed sequence of each group with the wild-type SgrS sequence i.e.
513 that of the plasmid used as error-prone PCR template.

514 We normalized the raw number of reads of each group by both the total number of reads and the
515 fraction of cells falling under each gate. As such, we defined a weighted average intensity to
516 each individual mutant along this 106 base long SgrS segment that we probed. Referred to as the
517 "intensity moment" from now on, we calculated the following quantity:

518

519 $$K_{ij} = \frac{\sum_{k=-2}^{2} \langle I_k \rangle c^k n_{ij}^k / N^k}{\sum_{k=-2}^{2} c^k n_{ij}^k / N^k} \qquad (1)$$

520

521 where, K_{ij} is the intensity moment of the mutant carrying a single substitution mutation at the i'th
522 base position to nucleotide type j rather than the wt base. c^k is the overall fraction of cells that
523 are sorted into the k'th bin based on the GFP intensity histogram that FACS acquisition
524 software reports. n^k is the number of reads carrying a single substitution mutation at base
525 position i to base type j and detected in the k'th FACS bin. N^k is the total number of acceptable
526 reads in the dataset. $N^k \geq \sum_{ij} n_{ij}^k$ due to experimental errors as well as reads carrying multiple
527 substitutions due to the stochastic nature of error-prone PCR. $\langle I_k \rangle$ is the median intensity of

528 the cells falling into the k'th bin as reported by FACS. For the representative intensity of
529 each bin, we used the median intensity reported by the FACS device.

530 In the figures, we reported the standard score of each entry given by

531 $$z = \frac{K_{ij} - \langle K_{ij} \rangle}{\sigma_{ij}(K_{ij})} \quad (2)$$

532 **Construction of bacterial strains**

533 The oligonucleotides, plasmids, and strains used in this study are listed in Supplementary Tables
534 1 and 2. *E. coli* K12 MG1655 derivatives were used for all experiments. P1 transduction[67] or λ-
535 red recombination[68] were used to move alleles between strains. DNA fragments were PCR
536 amplified using Q5® Hot Start High-Fidelity 2X Master Mix (NEB) and oligonucleotides
537 described in Supplementary Table 2. A set of plasmids (Supplementary Table 1) were used as
538 templates to PCR amplify the wild-type and *sgrS* mutants A177T, G178T, G178A, and G184A
539 using single-stranded oligos (Supplementary Table 2) containing 5' and 3´ homology to the
540 flanking regions of *cat-sacB* cassette (MB205). DNA fragments containing the *sgrS* mutants
541 G215A, T224G, T224A, T181A, and T182A were PCR amplified from MG1655 genomic DNA
542 using oligonucleotides listed in Supplementary Table 2.

543 Translational *ptsG'-'lacZ* reporter fusion under the control of the P_{BAD} promoter (strain MB130)
544 was constructed by PCR amplifying fragment of interest using primer pair MBP201F/MBP201R
545 containing 5' homologies to P_{BAD} and *lacZ.* PCR product was recombined into *E. coli* PM1205
546 using λ Red-mediated homologous recombination and counter-selection against *sacB* as
547 described previously[69]. Marked *λattB::lacI^q-PN25tetR-spec^R* was introduced into MB130 strain
548 by P1 *vir* transduction[70] to produce MB168 strain (Supplementary Table 1). Plasmid pZAMB1
549 harboring *sgrS* under the control of the $P_{LtetO-1}$ promoter was constructed by PCR amplifying

550 *sgrS* from *E. coli* MG1655 chromosomal DNA using oligonucleotides containing NdeI and
551 BamHI restriction sites. PCR products and vector pZA31R[71] were digested with NdeI and
552 BamHI (New England Biolabs) restriction endonucleases. Digestion products were ligated using
553 DNA Ligase (New England Biolabs) to produce plasmid containing $P_{LtetO-1}$-*sgrS* allele[40]. Single
554 nucleotide mutations in SgrS were introduced by QuikChange mutagenesis procedure using
555 oligonucleotides with mismatched bases at desired locations as following: A177T (A177T-F/
556 A177T-R), G178T (G178T-F/G178T-R), G178A (G178A-F/G178A-R), G184A (G184A-F/
557 G184A-R), G215A (G215A-F/ G215A-R), T224A (U224A-F/U224A-R), T224G (T224G-
558 F/T224G-R) (Supplementary Table 2).

559 **β-galactosidase assay**

560 Bacterial strains were cultured overnight in MOPS Rich medium with 25 μg ml^{-1}
561 chloramphenicol (Cm) and subcultured 1:100 to fresh MOPS Rich medium containing Cm and
562 0.0005% L-arabinose. Cells were grown at 37°C with shaking to OD_{600}~0.15 and 30 ng ml^{-1}
563 anhydrotetracycline (aTc) was added to induce expression of SgrS from the plasmid and cells
564 grown for another hour to OD_{600}~0.5. β-galactosidase assay was then performed according to
565 previously described protocol[70].

566 **Northern blot analysis**

567 Bacterial strains were cultured and β-galactosidase assay performed as described above.
568 Simultaneously, aliquots of the same culture were taken and total RNA was extracted as
569 described previously[72]. RNA concentrations were measured spectrophotometrically and 15 μg of
570 RNA were resolved on 6% polyacrylamide gel electrophoresis. RNA was transferred to 0.2 μm
571 pore-size Nytran N (Whatman) membrane as described previously[73]. Membrane was

572 prehybridized for 45 min in ULTRAhyb (Ambion) solution at 42°C. Blots were probed
573 overnight with 5'-biotinylated SgrS-bio or ssrA-bio probes specific for SgrS sRNA and 5S rRNA
574 respectively (Supplementary Table 2). BrightStar BioDetect kit (Ambion) was used for
575 detection. ImageJ (National Institutes of Health; [74]) was used to measure band densities from
576 four independent experiments.

577 **Measurement of intrinsic degradation rates of SgrS**

578 Strain DB166, MB206, MB209 and XM199 were cultured overnight at 37 °C and diluted 1:100
579 to a fresh LB medium and the cultures were grown at 37 °C to OD_{600} ~ 0.3. To induce SgrS
580 expression, αMG was added to final concentration of 0.5% and the cells were grown for
581 additional 30 minutes. Rifampicin was added to final concentration of 250 μg/ml and the cells
582 were grown for another 5 minutes. At this point, cells were harvested (t=0 timepoint) for RNA
583 extraction. Three biological replicates were harvested for each time-point.

584 Cells from 1.0 ml of culture were mixed with 2 ml of RNA protect reagent (Qiagen). The
585 mixture was pelleted at 4000 rpm for 10 minutes and then discard the supernatant. Total RNA
586 was isolated using Direct-Zol RNA miniPrep (Zymo) kit following the manufacturer's
587 instruction. Genomic DNA was removed by DNaseI provided by the Kit. Finally total RNA
588 was eluted in 40 μl of nuclease free water. First-strand cDNA was synthesized from 1 μg of total
589 RNA using Superscript™ IV First-Strand cDNA Synthesis SuperMix kit according to the
590 manufacturer's protocol (Invitrogen, USA).

591 The primers used to amplify SgrS are: OSA499 (GATGAAGCAAGGGGGTGCCC) and
592 OSA500 (CAATACTCAGTCACACATGATGCAGGC)

593 The primers used to amplify housekeeping gene *rrsA* are: OXM187
594 (ATTCCGATTAACGCTTGCAC) and OXM188 (AGGCCTTCGGGTTGTAAAGT)

595 Real-time PCR was performed using SYBR Green master mix (Fisher) and Eppendorf Realplex
596 in a 96-well plate. Each reaction is comprised of 1x SYBR Green master mix, 100 nM of each
597 primer, 2 μl of 1:50 diluted cDNA in a total of 10 μl reaction volumes. Each plate contains "no
598 template" controls for individual transcripts as well as housekeeping transcripts such as *rrsA* for
599 every sample as an internal control.

600 Delta delta Ct method was used to analyze the qPCR data. The transcripts turnover rates were
601 calculated based on the non-linear fit with one phase exponential decay curves using GraphPad
602 software.

603 **Cell culture, fixation and permeabilization for smFISH and super-resolution imaging**

604 The wild-type *E. coli* strain (DJ480) was grown overnight at 37 ºC, 250 rpm in LB Broth Miller
605 (EMD), the RNase E mutant was grown in 25 μg/ml kanamycin (Kan) (Fisher Scientific), the
606 SgrS A177U, G178U, G178A, U181A, U182A, G184A, G184A-C195U, G215A, U224A,
607 U224G mutants were grown in LB Broth with 50 μg/ml spectinomycin (Spec) (Sigma-Aldrich)
608 and the RNase E mutants of the respective SgrS mutations were grown in LB Broth with 25
609 μg/ml kanamycin and 50 μg/ml spectinomycin. The following day, the overnight cultures were
610 diluted 100-fold into MOPS EZ rich defined medium (Teknova) with 0.2% glucose and the
611 respective antibiotics, and allowed to grow at 37 ºC and 250 rpm until the OD_{600} reached 0.15-
612 0.25. α-methyl D-glucopyranoside (αMG) (Sigma-Aldrich) was used to introduce sugar-
613 phosphate stress and subsequently induce SgrS sRNA expression. A specific volume of liquid

614 was taken out of the culture after 0, 2, 4, 6, 8, 10, 15, 20 minutes of incubation and mixed with
615 formaldehyde (Fisher Scientific) to a final concentration of 4% for the fixation of the cells.

616 Δ*sgrS* and Δ*ptsG* strains were grown overnight in LB Broth Miller (EMD) at 37 ºC and 250 rpm
617 using 25 µg/ml kanamycin and 10 µg/ml tetracycline (Tet) (Sigma-Aldrich) respectively. The
618 next day the cultures were diluted 100-fold into MOPS EZ rich defined medium (Teknova) with
619 0.2% glucose (Sigma-Aldrich) and the respective antibiotics and left to grow at 37 ºC and 250
620 rpm again till the OD_{600} reached 0.2. The cells were then mixed with formaldehyde (Fisher
621 Scientific) to a final concentration of 4% to fix the cells.

622 Following the formaldehyde fixation, the cells were incubated at room temperature for 30
623 minutes and subsequently centrifuged at 3214 x g for 10 minutes at room temperature. The
624 pellets were resuspended in 200 µl 1X PBS and then washed 3 times, each time performing
625 centrifugation at 600 x g for 4 minutes and resuspending in 200 µl 1X PBS. The cells were then
626 permeabilized with 70% ethanol, shaken at room temperature for 1 hour and stored at 4 ºC prior
627 to fluorescence *in situ* hybridization.

628 **Single-molecule fluorescence *in situ* hybridization (smFISH)**

629 Stellaris Probe Designer was used to design the smFISH probes and they were ordered from
630 Biosearch Technologies (https://www.biosearchtech.com/). The probe labeling was performed
631 by using equal volumes of each probe. The final volume of sodium bicarbonate was adjusted to
632 0.1 M by adding 1/9 reaction volume of 1 M sodium bicarbonate (pH = 8.5). 0.05-0.25 mg of
633 Alexa Fluor 647 succinimidyl ester (Life Technologies) or CF 568 succinimidyl ester (Biotium)
634 dissolved in 5 µl DMSO was mixed with the probe solution. The dyes were kept at a molar
635 excess of 20-25 fold relative to the probes. The reaction mixture was incubated in the dark at 37

636 ºC with gentle vortexing overnight. The following day the reaction was quenched by using 1/9
637 reaction volume of 3 M sodium acetate (pH = 5). Ethanol precipitation followed by P-6 Micro
638 Bio-Spin Columns (Bio-Rad) were employed to remove unconjugated dyes.

639 60 µl of permeabilized cells were centrifuged at 600 x g for 4 minutes and the pellets were
640 washed with FISH wash solution (10% formamide in 2X Saline Sodium Citrate (SSC) buffer).
641 They were then resuspended along with the probes in 15 µl of FISH hybridization buffer (10%
642 dextran sulfate (Sigma-Aldrich), 1 mg/ml *E. coli* tRNA (Sigma-Aldrich), 0.2 mg/ml Bovine
643 Serum Albumin (BSA) (NEB), 2 mM vanadyl ribonucleoside complexes (Sigma-Aldrich), 10%
644 formamide (Fisher Scientific) in 2X SSC). The number of probes used for sRNA SgrS was 9,
645 they were labeled with Alexa Fluor 647 and the concentration of the labeled probes was 50 nM.
646 The number of probes used for *ptsG* mRNA was 28, they were labeled with CF 568 and the
647 labeled probe concentration was 15 nM. The reaction mixtures were incubated in the dark at 30
648 ºC overnight. The following day, the cells were suspended in 20X volume FISH wash solution
649 and centrifuged. They were resuspended in FISH wash solution, incubated at 30 ºC for 30
650 minutes and centrifuged, and this was repeated 3 times. After the final washing step, the cells
651 were pelleted and resuspended in 20 µl 4X SSC and stored at 4 ºC prior to imaging.

652 **Single-molecule localization-based super-resolution imaging**

653 The labeled cells were immobilized on 1.0 borosilicate chambered coverglass (Thermo Scientific
654 Nunc Lab-Tek) treated with poly-L-lysine (Sigma-Aldrich) and imaged with imaging buffer (50
655 mM Tris-HCl (pH = 8.0), 10% glucose (Sigma-Aldrich), 1% β-mercaptoethanol (Sigma-
656 Aldrich), 0.5 mg/ml glucose oxidase (Sigma-Aldrich) and 0.2% catalase (Sigma-Aldrich) in 2X
657 SSC).

658 3D super-resolution imaging was performed using an Olympus IX-71 inverted microscope with a
659 100X NA 1.4 SaPo oil immersion objective. Sapphire 568-100 CW CDRH (568 nm) (Coherent)
660 and DL-640-100-AL-O (647 nm) (Crystalaser) were used for two-color imaging and DL405-025
661 (405 nm) (Crystalaser) was used for the reactivation of the dyes. The laser excitation was
662 controlled by mechanical shutters (LS6T2, Uniblitz). The laser lines were reflected to the
663 objective using a dichroic mirror (Di01-R405/488/561/635, Semrock) The emission signal was
664 collected by the objective and then they passed through an emission filter (FF01-594/730-25,
665 Semrock for Alexa Fluor 647 or HQ585/70M 63061, Chroma for CF 568) and the excitation
666 laser was cleaned using notch filters (ZET647NF, Chroma; NF01-568/647-25x5.0, Semrock and
667 NF01-568U-25, Semrock). The images were captured on a 512x512 Andor EMCCD camera
668 (DV887ECS-BV, Andor Tech). 3D imaging was achieved by introducing astigmatism using a
669 cylindrical lens with focal length 2 m (SCX-50.8-1000.0-UV-SLMF-520-820, CVI Melles Griot)
670 in the emission path between two relay lenses of focal lengths 100 mm and 150 mm. Each pixel
671 corresponded to 100 nm in this setup. The z-drift of the setup was controlled by the CRISP
672 (Continuous Reflective Interface Sample Placement) system (ASI) and the region of interest for
673 imaging was selected using an xy-sample stage (BioPrecision2, Ludl Electronic Products). The
674 storm-control software written in Python by Zhuang's group and available at GitHub
675 (https://github.com/ZhuangLab/storm-control) was used for image acquisition.

676 After acquiring a DIC image of the sample area, two-color super-resolution imaging was
677 performed. 568 nm laser excitation was used for CF 568 after completing the image acquisition
678 for Alexa Fluor 647 using 647 nm laser excitation. Fluorophore bleaching was compensated and
679 moderate signal density was maintained by increasing the 405 nm laser power slowly. Imaging

680 was completed when most of the fluorophores had photobleached and the highest reactivation
681 laser power was reached.

682 Fluorescent nanodiamonds (140 nm diameter, Sigma Aldrich) were utilized for mapping of the
683 two channels. These nanodiamonds nonspecifically attached to the surface of the imaging
684 chambers and were excited by both 647 nm and 568 nm lasers. They generated localization spots
685 in the final reconstructed images that was used for mapping.

686 **Image Analysis**

687 The raw data was acquired using the Python-based acquisition software and it was analyzed
688 using a data analysis algorithm which was based on work published previously by Zhuang's
689 group.[75,76] The peak identification and fitting were performed using the method described
690 before.[34] The z-stabilization was done by the CRISP system and the horizontal drift was
691 calculated using Fast Fourier Transformation (FFT) on the reconstructed images of subsets of the
692 super-resolution image, comparing the center of the transformed images and corrected using
693 linear interpolation.

694 **Clustering Analysis and copy number calculation**

695 A density-based clustering analysis algorithm (DBSCAN) was employed to calculate the RNA
696 copy numbers. The algorithm used was the same as previously published,[34] but the Nps and Eps
697 values were updated for the SgrS and *ptsG* images, since, we used CF 568 instead of Alexa Fluor
698 568 and we also used a different 405 nm laser to reactivate the dyes. The SgrS (9 probes labeled
699 with Alexa Fluor 647) images were clustered using Nps = 3 and Eps = 15 and the *ptsG* (28
700 probes labeled with CF 568) images were clustered using Nps = 10 and Eps = 25 and these
701 numbers were empirically chosen. A MATLAB code was used as before for the cluster analysis.

702 Δ*sgrS* and Δ*ptsG* strains were grown, prepared, imaged and analyzed in the same manner as
703 before and they were used for the measurement of the background signal due to the non-specific
704 binding of Alexa Fluor 647 and CF 568.

705 The SgrS image with no αMG induction for the wild-type *E. coli* cells (DJ480) was considered to
706 be the low SgrS copy number sample, where it was assumed that one cluster was equivalent to
707 one RNA and the *ptsG* image with 20 minute αMG induction for the wild-type *E. coli* cells was
708 considered to be the low *ptsG* copy number sample. The copy numbers of the RNAs were
709 calculated in the same manner using MATLAB codes as described previously.[34]

710 **Colocalization analysis**

711 To calculate the copy number of SgrS-*ptsG* complexes, colocalization analysis was performed in
712 order to calculate the percentage of *ptsG* colocalized with SgrS. The average radius of a *ptsG*
713 mRNA cluster was calculated to be around 40 nm. That value was used as the radius to consider
714 a 3D spherical volume from the center of the *ptsG* cluster. The SgrS spots corresponding to
715 clusters found in this volume were taken to be colocalized with the *ptsG* cluster. The base-
716 pairing mutant strain was considered a negative control (Supplementary Fig. 41a) and percentage
717 of colocalization was plotted against SgrS copy number and fit with a line (y = a*x) to act as a
718 calibration for colocalization by chance (Supplementary Fig. 41b). The coefficient, a, was used a
719 correction factor for colocalization calculation as, final colocalization = calculated colocalization
720 – a*SgrS copy number.

721 **SgrS and *ptsG* mRNA half-life measurements**

722 The *ptsG* mRNA degradation rates were calculated using a rifampicin-chase experiment. The
723 wild-type (DJ480) *E. coli* cells, the SgrS A177U, G178A, G178U, U181A, U182A, G184A,

724 G184A-C195U, G215A, U224A, and U224G were grown in LB Broth with the respective
725 antibiotics at 37 ºC, 250 rpm overnight. The following day, the overnight cultures were diluted
726 100-fold in MOPS EZ rich defined medium supplemented with 0.2% glucose and they were
727 grown at 37 ºC, 250 rpm. When the OD_{600} reached 0.15-0.25 rifampicin (Sigma-Aldrich) was
728 added to a final concentration of 500 µg/ml. This was taken as the 0-minute time point for the
729 experiment and aliquots were taken at 2, 4, 6, 8, 10, 15, 20 minutes after the addition of
730 rifampicin and fixed in the same manner described before. The cells were labeled by FISH
731 probes, imaged and analyzed by the same process mentioned. The natural logs of the copy
732 numbers were plotted against time and the slope of the linear fitting was used to calculate the
733 lifetime of the RNA. The reciprocal of the lifetimes gave the degradation rates.

734 The SgrS degradation rates were calculated for the above strains and the wild-type Δ*hfq*, A177U
735 Δ*hfq*, G184A Δ*hfq* mutants by stopping the transcription of SgrS by removing αMG from the
736 media. The wild-type *E. coli* cells, the mutants and the RNase E mutants were grown overnight
737 as described before in LB Broth with the respective antibiotics. The cells were diluted the
738 following day and grown in MOPS EZ rich defined medium with the respective antibiotics till
739 OD_{600} 0.15-0.25. SgrS transcription was induced in the cells using αMG and growing them for
740 10 minutes. The cells were then washed twice with centrifugation and resuspension with cold,
741 fresh media devoid of αMG and finally resuspended in pre-warmed media at 37 ºC. Aliquots
742 were taken at 0, 2, 4, 6, 8, 10, 15, 20 minutes (0, 2, 4, 6, 8 minutes for the Δ*hfq* strains) and fixed
743 as described before. The cells were then treated, imaged and analyzed to calculate the
744 degradation rates as mentioned before.

745 **Modeling of SgrS-induced *ptsG* mRNA degradation**

746 <u>Kinetic model and experimental measurements of the parameters</u>

747 The mass-action equations used for the wild-type *E. coli* cells and the chromosomal mutations
748 are shown below:

749 $$\frac{d[p]}{dt} = \alpha_p - \beta_p[p] - k_{on}[S][p] + k_{off}[Sp] \qquad (3)$$

750 $$\frac{d[S]}{dt} = \alpha_S - \beta_{S,p}[S] - k_{on}[S][p] + k_{off}[Sp] \qquad (4)$$

751 $$\frac{d[Sp]}{dt} = k_{on}[S][p] - k_{off}[Sp] - k_{cat}[Sp] \qquad (5)$$

752 In the above equations, the changes in the concentration of *ptsG*, SgrS and the SgrS-*ptsG*
753 complex over time are shown. α_p, α_S are the transcription rates of the *ptsG* mRNA and SgrS
754 respectively; $\beta_p, \beta_{S,p}$ are respectively the endogenous degradation rate of ptsG mRNA and the
755 degradation rate of SgrS excluding the co-degradation with *ptsG* mRNA; k_{on}, k_{off} are the rates
756 of association and dissociation of SgrS and *ptsG* mRNA and k_{cat} is the RNase E-mediated co-
757 degradation of SgrS-*ptsG* complex.

758 We calculated the endogenous degradation rate of *ptsG* mRNA (β_p) of the wild-type *E. coli*,
759 chromosomal mutations and the RNase E mutants from the super-resolution imaging and
760 analysis. The degradation rate of SgrS for the cells were calculated by stopping the transcription
761 of SgrS, but this method takes into account target-dependent and target-independent degradation
762 ($\beta_{S,total}$). We also calculated the degradation rate for the respective RNase E mutant strains and
763 this measurement gave us target-independent degradation and other RNase E–independent
764 degradation (β_{S0}). These two values provided a higher and lower bound for the endogenous
765 degradation rate of SgrS ($\beta_{S,p}$).

766 The transcription rate of *ptsG* mRNA was calculated using $\alpha_p = \beta_p \times [p]_0$ and in this equation
767 $[p]_0$ is the concentration of *ptsG* mRNA before the induction of sugar stress in all of the cases.
768 This was done because it was observed previously[34] that the *ptsG* mRNA reached an equilibrium
769 in the cells without SgrS-induced degradation. We calculated this for all the cases, viz., wild-type
770 *E. coli*, SgrS mutants and the RNase E mutants and the transcription rate of *ptsG* mRNA did not
771 show any significant change.

772 RNase E mutant cells are not able to degrade SgrS-*ptsG* complex efficiently, but it is a
773 possibility that the complex can degrade endogenously or via other minor degradation pathways.
774 We kept k_{cat} as a fitting parameter and used the measured parameters, α_p, β_p, $\beta_{S,total}$and β_{S0}
775 and the above equations to fit the time courses for all the strains to estimate the 5 parameters; α_S,
776 $\beta_{S,p}$, k_{on}, k_{off} and k_{cat}.

777 <u>Parameter search</u>

778 Poisson weighting (total sum of the squares, $SS_{tot} = \Sigma_i(y_i - \bar{y})^2$ and residual sum of the
779 squares, $SS_{res} = \Sigma_i(y_i - f_i)^2$, where y_i is the experimental data and f_i is the fitted data) was
780 used in the fitting of global R^2 according to the equation:

781 $$R^2 \equiv 1 - \frac{SS_{res}}{SS_{tot}} \qquad (6)$$

782 so that no bias was introduced for a particular species. The parameters were selected to maximize
783 the global R^2 for the time course curves of each of the species. The concentrations of the SgrS-
784 *ptsG* complex in all the strains were very close to the background and as a result the total
785 variance became small. R^2 was not helpful to estimate the quality of the fit in these cases.
786 Instead, χ^2's were calculated as

$$\chi^2 \equiv \sum_i \frac{(y_i - f_i)^2}{f_i} \qquad (7)$$

for all those cases and the significance levels (α) were reported.

References

1. Malkova, A. & Ira, G. Break-induced replication: Functions and molecular mechanism. *Current Opinion in Genetics and Development* (2013). doi:10.1016/j.gde.2013.05.007

2. Geisler, S. & Coller, J. RNA in unexpected places: Long non-coding RNA functions in diverse cellular contexts. *Nature Reviews Molecular Cell Biology* (2013). doi:10.1038/nrm3679

3. Storz, G., Vogel, J. & Wassarman, K. M. Regulation by Small RNAs in Bacteria: Expanding Frontiers. *Molecular Cell* **43**, 880–891 (2011).

4. Wiedenheft, B., Sternberg, S. H. & Doudna, J. A. RNA-guided genetic silencing systems in bacteria and archaea. *Nature* (2012). doi:10.1038/nature10886

5. Askari, F. K. & McDonnell, W. M. Antisense-Oligonucleotide Therapy. *N. Engl. J. Med.* **334**, 316–318 (1996).

6. Singh, D. *et al.* Real-time observation of DNA target interrogation and product release by the RNA-guided endonuclease CRISPR Cpf1 (Cas12a). *Proc. Natl. Acad. Sci. U. S. A.* **115**, 5444–5449 (2018).

7. Singh, D., Sternberg, S. H., Fei, J., Doudna, J. A. & Ha, T. Real-time observation of DNA recognition and rejection by the RNA-guided endonuclease Cas9. *Nat. Commun.* **7**, 1–8

807 (2016).

808 8. Globyte, V., Lee, S. H., Bae, T., Kim, J. & Joo, C. CRISPR /Cas9 searches for a
809 protospacer adjacent motif by lateral diffusion . *EMBO J.* **38**, (2019).

810 9. Globyte, V., Kim, S. H. & Joo, C. Single-Molecule View of Small RNA–Guided Target
811 Search and Recognition. *Annu. Rev. Biophys.* **47**, 569–593 (2018).

812 10. Ragunathan, K., Liu, C. & Ha, T. RecA filament sliding on DNA facilitates homology
813 search. *Elife* **2012**, (2012).

814 11. Lee, J. Y. *et al.* Base triplet stepping by the Rad51/RecA family of recombinases. *Science*
815 *(80-.).* **349**, 977–981 (2015).

816 12. Qi, Z. *et al.* DNA sequence alignment by microhomology sampling during homologous
817 recombination. *Cell* **160**, 856–869 (2015).

818 13. Jones, D. L. *et al.* Kinetics of dCas9 target search in Escherichia coli. *Science (80-.).* **357**,
819 1420–1424 (2017).

820 14. Richards, G. R. & Vanderpool, C. K. Molecular call and response: The physiology of
821 bacterial small RNAs. *Biochimica et Biophysica Acta - Gene Regulatory Mechanisms*
822 **1809**, 525–531 (2011).

823 15. Desnoyers, G., Bouchard, M. P. & Massé, E. New insights into small RNA-dependent
824 translational regulation in prokaryotes. *Trends in Genetics* **29**, 92–98 (2013).

825 16. Massé, E., Vanderpool, C. K. & Gottesman, S. Effect of RyhB Small RNA on Global Iron
826 Use in Escherichia coli. *J. Bacteriol.* **187**, 6962–6971 (2005).

827 17. Lease, R. A., Smith, D., McDonough, K. & Belfort, M. The small noncoding DsrA RNA

828 is an acid resistance regulator in Escherichia coli. *J. Bacteriol.* **186**, 6179–6185 (2004).

829 18. Domenech, P., Honoré, N., Heym, B. & Cole, S. T. Role of OxyS of Mycobacterium
830 tuberculosis in oxidative stress: Overexpression confers increased sensitivity to organic
831 hydroperoxides. *Microbes Infect.* **3**, 713–721 (2001).

832 19. Zhang, A. *et al.* Global analysis of small RNA and mRNA targets of Hfq. *Mol. Microbiol.*
833 **50**, 1111–1124 (2003).

834 20. Bobrovskyy, M. & Vanderpool, C. K. The small RNA SgrS: Roles in metabolism and
835 pathogenesis of enteric bacteria. *Frontiers in Cellular and Infection Microbiology* **4**,
836 (2014).

837 21. Richards, G. R., Patel, M. V., Lloyd, C. R. & Vanderpool, C. K. Depletion of glycolytic
838 intermediates plays a key role in glucose-phosphate stress in escherichia coli. *J. Bacteriol.*
839 **195**, 4816–4825 (2013).

840 22. Bobrovskyy, M. *et al.* Determinants of target prioritization and regulatory hierarchy for
841 the bacterial small RNA SgrS. *Mol. Microbiol.* (2019). doi:10.1111/mmi.14355

842 23. Rice, J. B. & Vanderpool, C. K. The small RNA SgrS controls sugar-phosphate
843 accumulation by regulating multiple PTS genes. *Nucleic Acids Res.* **39**, 3806–3819
844 (2011).

845 24. Kawamoto, H., Koide, Y., Morita, T. & Aiba, H. Base-pairing requirement for RNA
846 silencing by a bacterial small RNA and acceleration of duplex formation by Hfq. *Mol.*
847 *Microbiol.* **61**, 1013–1022 (2006).

848 25. Panja, S. & Woodson, S. A. Hfq proximity and orientation controls RNA annealing.

849 *Nucleic Acids Res.* (2012). doi:10.1093/nar/gks618

850 26. Zuzanna, W. & Mikolaj, O. Hfq assists small RNAs in binding to the coding sequence of
851 ompD mRNA and in rearranging its structure. *RNA* **22**, 979–994 (2016).

852 27. Ishikawa, H., Otaka, H., Maki, K., Morita, T. & Aiba, H. The functional Hfq-binding
853 module of bacterial sRNAs consists of a double or single hairpin preceded by a U-rich
854 sequence and followed by a 3′ poly(U) tail. *RNA* **18**, 1062–1074 (2012).

855 28. Morita, T., Nishino, R. & Aiba, H. Role of the terminator hairpin in the biogenesis of
856 functional Hfq-binding sRNAs. *RNA* **23**, 1419–1431 (2017).

857 29. Otaka, H., Ishikawa, H., Morita, T. & Aiba, H. PolyU tail of rho-independent terminator
858 of bacterial small RNAs is essential for Hfq action. *Proc. Natl. Acad. Sci. U. S. A.* **108**,
859 13059–13064 (2011).

860 30. Horler, R. S. P. & Vanderpool, C. K. Homologs of the small RNA SGRS are broadly
861 distributed in enteric bacteria but have diverged in size and sequence. *Nucleic Acids Res.*
862 **37**, 5465–5476 (2009).

863 31. Maki, K., Uno, K., Morita, T. & Aiba, H. RNA, but not protein partners, is directly
864 responsible for translational silencing by a bacterial Hfq-binding small RNA. *Proc. Natl.*
865 *Acad. Sci. U. S. A.* **105**, 10332–10337 (2008).

866 32. Soper, T. J. & Woodson, S. A. The rpoS mRNA leader recruits Hfq to facilitate annealing
867 with DsrA sRNA. *RNA* (2008). doi:10.1261/rna.1110608

868 33. Maki, K., Morita, T., Otaka, H. & Aiba, H. A minimal base-pairing region of a bacterial
869 small RNA SgrS required for translational repression of ptsG mRNA. *Mol. Microbiol.* **76**,

870 782–792 (2010).

871 34. Fei, J. *et al.* Determination of in vivo target search kinetics of regulatory noncoding RNA.
872 *Science (80-.).* **347**, 1371–1374 (2015).

873 35. Arluison, V. *et al.* Spectroscopic observation of RNA chaperone activities of Hfq in post-
874 transcriptional regulation by a small non-coding RNA. *Nucleic Acids Res.* (2007).
875 doi:10.1093/nar/gkl1124

876 36. Hwang, W., Arluison, V. & Hohng, S. Dynamic competition of DsrA and rpoS fragments
877 for the proximal binding site of Hfq as a means for efficient annealing. *Nucleic Acids Res.*
878 (2011). doi:10.1093/nar/gkr075

879 37. Rutherford, S. T., Valastyan, J. S., Taillefumier, T., Wingreen, N. S. & Bassler, B. L.
880 Comprehensive analysis reveals how single nucleotides contribute to noncoding RNA
881 function in bacterial quorum sensing. *Proc. Natl. Acad. Sci. U. S. A.* **112**, (2015).

882 38. Kinney, J. B., Murugan, A., Callan, C. G. & Cox, E. C. Using deep sequencing to
883 characterize the biophysical mechanism of a transcriptional regulatory sequence. *Proc.*
884 *Natl. Acad. Sci. U. S. A.* **107**, 9158–9163 (2010).

885 39. Peterman, N., Lavi-Itzkovitz, A. & Levine, E. Large-scale mapping of sequence-function
886 relations in small regulatory RNAs reveals plasticity and modularity. *Nucleic Acids Res.*
887 **42**, 12177–12188 (2014).

888 40. Bobrovskyy, M. & Vanderpool, C. K. Diverse mechanisms of post-transcriptional
889 repression by the small RNA regulator of glucose-phosphate stress. *Mol. Microbiol.* **99**,
890 254–273 (2016).

891 41. Wadler, C. S. & Vanderpool, C. K. A dual function for a bacterial small RNA: SgrS
892 performs base pairing-dependent regulation and encodes a functional polypeptide. *Proc.*
893 *Natl. Acad. Sci.* **104**, 20454–20459 (2007).

894 42. Balasubramanian, D. & Vanderpool, C. K. Deciphering the interplay between two
895 independent functions of the small RNA regulator SgrS in Salmonella. *J. Bacteriol.*
896 (2013). doi:10.1128/JB.00586-13

897 43. Morita, T., Ueda, M., Kubo, K. & Aiba, H. Insights into transcription termination of Hfq-
898 binding sRNAs of Escherichia coli and characterization of readthrough products. *RNA* **21**,
899 1490–1501 (2015).

900 44. De Lay, N., Schu, D. J. & Gottesman, S. Bacterial small RNA-based negative regulation:
901 Hfq and its accomplices. *Journal of Biological Chemistry* **288**, 7996–8003 (2013).

902 45. Sun, Y. & Vanderpool, C. K. Physiological consequences of multiple-target regulation by
903 the small RNA SgrS in escherichia coli. *J. Bacteriol.* **195**, 4804–4815 (2013).

904 46. Rice, J. B., Balasubramanian, D. & Vanderpool, C. K. Small RNA binding-site
905 multiplicity involved in translational regulation of a polycistronic mRNA. *Proc. Natl.*
906 *Acad. Sci. U. S. A.* **109**, (2012).

907 47. Wadler, C. S. & Vanderpool, C. K. Characterization of homologs of the small rna sgrs
908 reveals diversity in function. *Nucleic Acids Res.* **37**, 5477–5485 (2009).

909 48. Gottesman, S. & Storz, G. Bacterial small RNA regulators: Versatile roles and rapidly
910 evolving variations. *Cold Spring Harb. Perspect. Biol.* **3**, (2011).

911 49. Aiba, H. Mechanism of RNA silencing by Hfq-binding small RNAs. *Current Opinion in*

912 *Microbiology* **10**, 134–139 (2007).

913 50. Sauer, E. & Weichenrieder, O. Structural basis for RNA 3′-end recognition by Hfq. *Proc.*
914 *Natl. Acad. Sci. U. S. A.* **108**, 13065–13070 (2011).

915 51. Panja, S., Schu, D. J. & Woodson, S. A. Conserved arginines on the rim of Hfq catalyze
916 base pair formation and exchange. *Nucleic Acids Res.* (2013). doi:10.1093/nar/gkt521

917 52. Panja, S., Paul, R., Greenberg, M. M. & Woodson, S. A. Light-Triggered RNA Annealing
918 by an RNA Chaperone. *Angew. Chemie Int. Ed.* **54**, 7281–7284 (2015).

919 53. Mann, M., Wright, P. R. & Backofen, R. IntaRNA 2.0: Enhanced and customizable
920 prediction of RNA-RNA interactions. *Nucleic Acids Res.* **45**, W435–W439 (2017).

921 54. Wright, P. R. *et al.* CopraRNA and IntaRNA: Predicting small RNA targets, networks and
922 interaction domains. *Nucleic Acids Res.* **42**, (2014).

923 55. Busch, A., Richter, A. S. & Backofen, R. IntaRNA: Efficient prediction of bacterial sRNA
924 targets incorporating target site accessibility and seed regions. *Bioinformatics* **24**, 2849–
925 2856 (2008).

926 56. Raden, M. *et al.* Freiburg RNA tools: A central online resource for RNA-focused research
927 and teaching. *Nucleic Acids Res.* **46**, W25–W29 (2018).

928 57. Morita, T., Maki, K. & Aiba, H. RNase E-based ribonucleoprotein complexes: Mechanical
929 basis of mRNA destabilization mediated by bacterial noncoding RNAs. *Genes Dev.* **19**,
930 2176–2186 (2005).

931 58. Bruce, H. A. *et al.* Analysis of the natively unstructured RNA/protein-recognition core in
932 the Escherichia coli RNA degradosome and its interactions with regulatory RNA/Hfq

933 complexes. *Nucleic Acids Res.* **46**, 387–402 (2018).

934 59. Caillet, J., Baron, B., Boni, I. V., Caillet-Saguy, C. & Hajnsdorf, E. Identification of
935 protein-protein and ribonucleoprotein complexes containing Hfq. *Sci. Rep.* **9**, 1–12 (2019).

936 60. Updegrove, T. B., Zhang, A. & Storz, G. Hfq: The flexible RNA matchmaker. *Current*
937 *Opinion in Microbiology* **30**, 133–138 (2016).

938 61. Schu, D. J., Zhang, A., Gottesman, S. & Storz, G. Alternative Hfq- sRNA interaction
939 modes dictate alternative mRNA recognition . *EMBO J.* (2015).
940 doi:10.15252/embj.201591569

941 62. Dimastrogiovanni, D. *et al.* Recognition of the small regulatory RNA RydC by the
942 bacterial Hfq protein. *Elife* **3**, (2014).

943 63. Geissmann, T. A. & Touati, D. Hfq, a new chaperoning role: Binding to messenger RNA
944 determines access for small RNA regulator. *EMBO J.* **23**, 396–405 (2004).

945 64. Peng, Y., Curtis, J. E., Fang, X. & Woodson, S. A. Structural model of an mRNA in
946 complex with the bacterial chaperone Hfq. *Proc. Natl. Acad. Sci. U. S. A.* **111**, 17134–
947 17139 (2014).

948 65. Storz, G., Opdyke, J. A. & Zhang, A. Controlling mRNA stability and translation with
949 small, noncoding RNAs. *Current Opinion in Microbiology* **7**, 140–144 (2004).

950 66. Valentin-Hansen, P., Eriksen, M. & Udesen, C. The bacterial Sm-like protein Hfq: A key
951 player in RNA transactions. *Molecular Microbiology* **51**, 1525–1533 (2004).

952 67. Miller, J. H. *Experiments in molecular genetics*. ((Cold Spring Harbor, N.Y.: Cold Spring
953 Harbor Laboratory, 1972).

954 68. Yu, D. *et al.* An efficient recombination system for chromosome engineering in
955 Escherichia coli. *Proc. Natl. Acad. Sci. U. S. A.* **97**, 5978–5983 (2000).

956 69. Mandin, P. & Gottesman, S. A genetic approach for finding small RNAs regulators of
957 genes of interest identifies RybC as regulating the DpiA/DpiB two-component system.
958 *Mol. Microbiol.* **72**, 551–565 (2009).

959 70. Miller, J. H. *Experiments in Molecular Genetics.* . (Cold Spring Harbor Laboratory, Cold
960 Spring Harbor, New York, 1972).

961 71. Levine, E., Zhang, Z., Kuhlman, T. & Hwa, T. Quantitative characteristics of gene
962 regulation by small RNA. *PLoS Biol.* (2007). doi:10.1371/journal.pbio.0050229

963 72. Aiba, H., Adhya, S. & de Crombrugghe, B. Evidence for two functional gal promoters in
964 intact Escherichia coli cells. *J. Biol. Chem.* **256**, 11905–10 (1981).

965 73. Majdalani, N., Chen, S., Murrow, J., St. John, K. & Gottesman, S. Regulation of RpoS by
966 a novel small RNA: The characterization of RprA. *Mol. Microbiol.* (2001).
967 doi:10.1046/j.1365-2958.2001.02329.x

968 74. Schneider, C. A., Rasband, W. S. & Eliceiri, K. W. NIH Image to ImageJ: 25 years of
969 image analysis. *Nature Methods* (2012). doi:10.1038/nmeth.2089

970 75. Rust, M. J., Bates, M. & Zhuang, X. Sub-diffraction-limit imaging by stochastic optical
971 reconstruction microscopy (STORM). *Nat. Methods* **3**, 793–5 (2006).

972 76. Huang, B., Wang, W., Bates, M. & Zhuang, X. Three-dimensional super-resolution
973 imaging by stochastic optical reconstruction microscopy. *Science (80-.).* **319**, 810–813
974 (2008).

975

976 **Acknowledgements**

977 We would like to thank Erel Levine, Divya Balasubramanian, and D. Jin for plasmids and
978 strains. We thank Hao Zhang at the Cell Sorting Core Facility (Bloomberg School of Public
979 Health) for helping us with the flow cytometry and sorting experiments. We appreciate and thank
980 Prof. Sarah Woodson for going through the manuscript and providing insightful suggestions.
981 This work was supported by grants from National Institutes of Health R01 GM112659 (M.B.,
982 M.S.A., T.H., J.Z., and A.P.), R35 GM122569 (T.H., J.Z., and A.P.), National Science
983 Foundation PHY 1430124 (T.H., J.Z., and A.P). T.H. is an investigator with the Howard Hughes
984 Medical Institute.

985

986 **Author Contributions**

987 A.P., C.K.V., T.H. designed the experiments, with help from M.B. and J.Z. A.P., T.K., and J.Z.
988 performed the Sort-Seq experiments and the Sort-Seq data was analyzed by A.P., T.K., and P.L.
989 M.B. performed the β-galactosidase and Northern blot experiments. M.S.A. and X.M. made the
990 strains that were used in this work. M.S.A. and X.M. performed the qPCR experiments to
991 calculate RNA lifetimes. A.P. performed all super-resolution imaging experiments, with some
992 help from J.Z. A.P. performed the analysis for the imaging experiments with the MATLAB
993 package written by D.S. and J.F. A.P., Z.L.S, C.K.V., and T.H. discussed the data. A.P., T.K.,
994 M.S.A., X.M., J.F., C.K.V., and T.H. wrote the manuscript.

995

996 **Competing Interests**

997 The authors declare no competing interests.

998

999 **Figure Legends**

1000 **Figure 1. Target search kinetics of SgrS. (a)** Kinetic scheme of *ptsG* mRNA degradation
1001 induced by wild-type SgrS sRNA and the different SgrS point mutants . The figure shows one of
1002 the SgrS mutant strains, A177U. The steps are described in detail in the main text and the inset
1003 shows the mutants used in this study. [*p*], [*S*] and [*Sp*] are the concentrations of *ptsG* mRNA,
1004 SgrS and the SgrS-*ptsG* complex, respectively, in their mass-action equations. **(b)** Secondary
1005 structure of SgrS sRNA from nucleotide 168 to the poly-U tail. The nucleotide positions where
1006 mutations were made are boxed. The nucleotides involved in base pairing with *ptsG* mRNA are
1007 red. **(c)** Base-pairing interaction between SgrS and *ptsG* mRNA showing the complementary
1008 region, start site and ribosome binding site.

1009 **Figure 2. Mapping efficacy of SgrS regulation of ptsG mRNA with respect to its sequence.**
1010 **(a)** Preparation of SgrS mutation library. Mutations were introduced into the SgrS plasmid using
1011 mutagenesis PCR. This library was then transformed into an *E. coli* strain already transformed
1012 with the *ptsG* mRNA plasmid fused with a GFP reporter. **(b)** Sorting of the cells and sequencing.
1013 The cells with two-plasmid co-expression were sorted using flow cytometry. The SgrS library
1014 (blue) shows GFP fluorescence that spans the region from the wild-type SgrS (black) to target
1015 (*ptsG*)-only (green). Cells were sorted into 5 evenly spaced (log scale) fluorescence bins and the
1016 occupancy percentages were 18.74%, 33.76%, 30.91%, 13.83% and 2.76% respectively. The
1017 cells from each bin were grown, DNA was purified, barcoded and sequenced using Illumina

1018 sequencing platform. **(c)** Histogram of the Sort-Seq measurements from the SgrS library from
1019 two replicates combined. The mean fluorescence for the wild-type SgrS is shown in red. **(d)** Heat
1020 map showing the effect of mutations on SgrS regulation of *ptsG* mRNA starting from nucleotide
1021 149 to 227. The colors in the boxes are scaled from blue (low) to red (high), according to the
1022 level of perturbation of SgrS regulation. Black squares represent the wild-type base at each
1023 position and the black boxes with white crosses show the position of the mutants missing in the
1024 experiment. Text shows the wild type sequence of SgrS. Insets show the four regions of SgrS,
1025 viz. base-pairing region, small stem-loop, terminator stem-loop and the poly-U tail.

1026 **Figure 3. Regulation of *ptsG'-'lacZ* translational fusion by SgrS point-mutants. (a)**
1027 Regulation of chromosomal *ptsG'-'lacZ* translational fusion by wild-type SgrS and A177U,
1028 G178U, G178A, G184A, G215A, U224A, U224G mutant variants (plasmid-encoded) was
1029 assessed using β-galactosidase activity assay. Standard error was calculated based on data from
1030 four biological replicates. **(b)** RNA was extracted simultaneously with β-galactosidase activity
1031 assay and Northern blot was performed using probes specific for SgrS sRNA and 5S rRNA
1032 (control). Full-length (227 nt), properly terminated SgrS transcripts are labeled as "termination"
1033 products, and longer transcripts that arose due to transcriptional readthrough are labeled as
1034 "readthrough" products. **(c)** Band intensities of total SgrS transcripts (termination+readthrough)
1035 were measured, and 5S-normalized values were plotted as "SgrS abundance" (steady state
1036 transcript abundance of SgrS mutants). **(d)** Band intensities of SgrS termination and readthrough
1037 products were measured and 5S-normalized ratios (readthrough/termination) were calculated and
1038 plotted for each SgrS mutant as "SgrS readthrough ratio".

1039 **Figure 4. 3D super-resolution images projected in 2D planes.** The panels show SgrS (red) and
1040 *ptsG* mRNA (green) labeled by smFISH for the wild-type and the mutant strains, A177U,

1041 G178A, G178U, U181A, U182A, G184A, G184A-C195U, G215A, U224A, U224G before and
1042 after 20 minutes of αMG (non-metabolizable sugar analogue) induction. Cell boundaries are
1043 denoted by white solid lines. Scale bar is 2 μm.

1044 **Figure 5. Time dependent changes in the copy numbers of SgrS and *ptsG* mRNA and**
1045 **estimation of kinetic parameters.** Time course changes and corresponding modeling curves for
1046 the SgrS, *ptsG* mRNA and SgrS-*ptsG* complex in **(a)** wild-type, **(c)** G184A mutant strain, **(e)**
1047 G184A-C195U mutant strain, **(g)** G215A mutant strain. Average copy numbers per cell are
1048 plotted against time. Rate constants obtained for these mutants are shown in Figure 6 and in
1049 Supplementary Table 3. Weighted R^2's for modeling are also reported in Supplementary Table 4.
1050 Error bars in **(a)**, **(c)**, **(e)**, **(g)** are standard errors from 80 to 150 cells in each case. Histograms
1051 showing the change in distribution of SgrS and *ptsG* mRNA copy numbers for **(b)** wild-type, **(d)**
1052 G184A mutant strain, **(f)** G184A-C195U mutant strain, **(h)** G215A mutant strain for 80-150 cells
1053 in each case.

1054 **Figure 6. Calculation of various parameters and correlation with Sort-Seq. (a)** Degradation
1055 rates of SgrS for the wild-type and the strains A177U, G178A, G178U, U181A, U182A, G184A,
1056 G184A-C195U, G215A, U224A, U224G, Δ*hfq* wild type, Δ*hfq* A177U, Δ*hfq* G184A for full
1057 length RNase E and RNase E mutants. Error bars represent standard deviation from two
1058 experimental replicates. **(b-d)** k_{on}, k_{off}, K_D measured from the time dependent modeling curves of
1059 the SgrS, *ptsG* mRNA and SgrS-*ptsG* mRNA complexes for the wild-type and strains A177U,
1060 G178A, G178U, U181A, U182A, G184A, G184A-C195U, G215A, U224A, U224G. These were
1061 determined simultaneously in the wild-type and RNase E mutants. Error bars report standard
1062 deviation from the independent fitting on two replicates. **(e)** Time course changes in *ptsG* mRNA
1063 for the wild-type, G184A, G184A-C195U, G215A mutant strains. Error bars represent standard

1064 errors from 80-150 cells in each case. **(f)** Fractional change in *ptsG* mRNA copy numbers for the
1065 wild-type and the mutants A177U, G178A, G178U, U181A, U182A, G184A, G184A-C195U,
1066 G215A, U224A, U224G before and after 20 minutes αMG induction. Error bars represent
1067 standard errors from 80-150 cells in each case. **(g)** Comparison of the SgrS regulation efficacy
1068 calculated from Sort-Seq assay and the imaging-based analysis. Error bars in the x-axis are
1069 standard deviations calculated from two experimental replicates and those in the y-axis are as
1070 described in **(f)**. The fitting is shown in blue and the grey region shows the 95% confidence
1071 region.

a

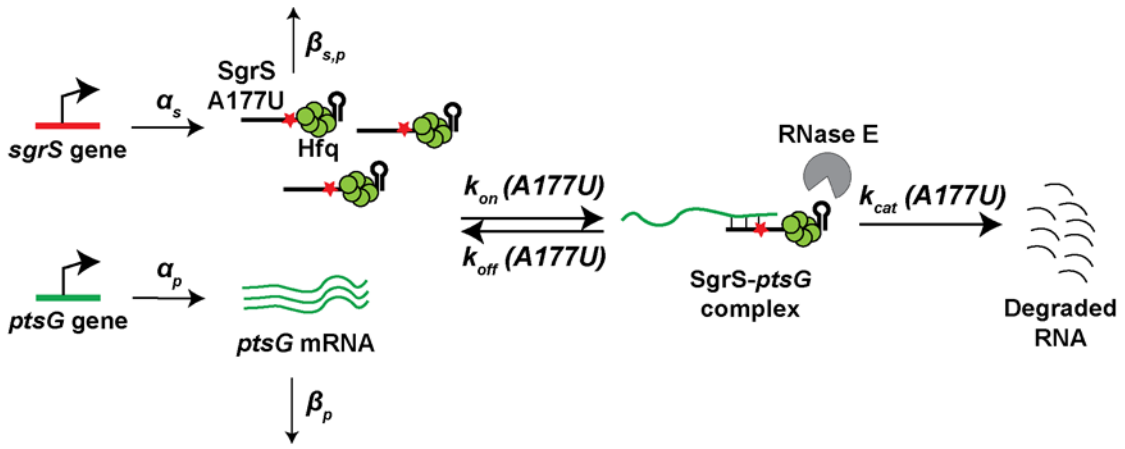

$$\frac{d[p]}{dt} = \alpha_p - \beta_p[p] - k_{on}[S][p] + k_{off}[Sp]$$

$$\frac{d[S]}{dt} = \alpha_S - \beta_{S,p}[S] - k_{on}[S][p] + k_{off}[Sp]$$

$$\frac{d[Sp]}{dt} = k_{on}[S][p] - k_{off}[Sp] - k_{cat}[Sp]$$

Mutants used in this study

A177U	G184A
G178A	G184A-C195U
G178U	G215A
U181A	U224A
U182A	U224G

b

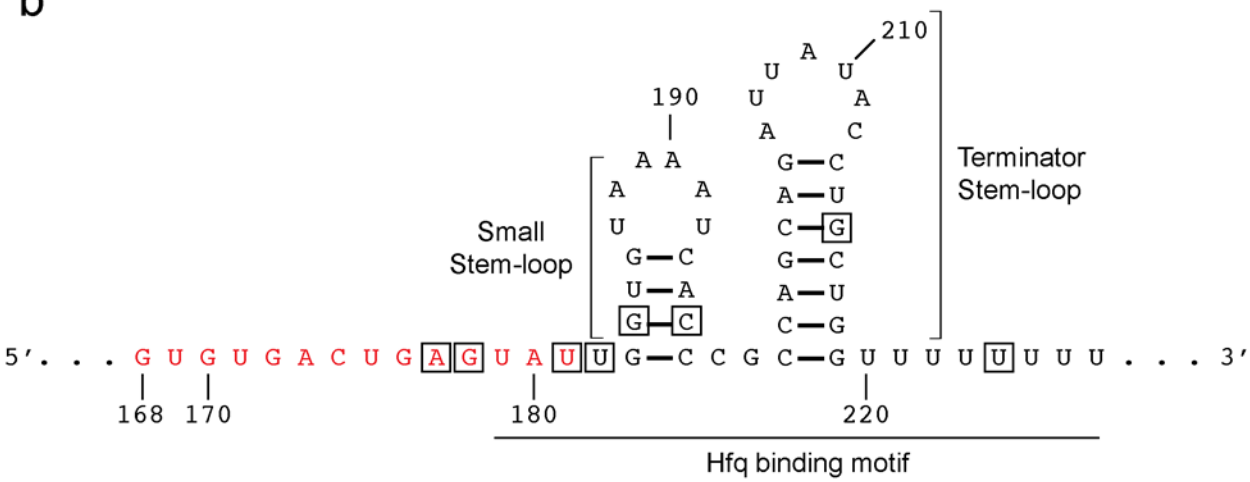

c

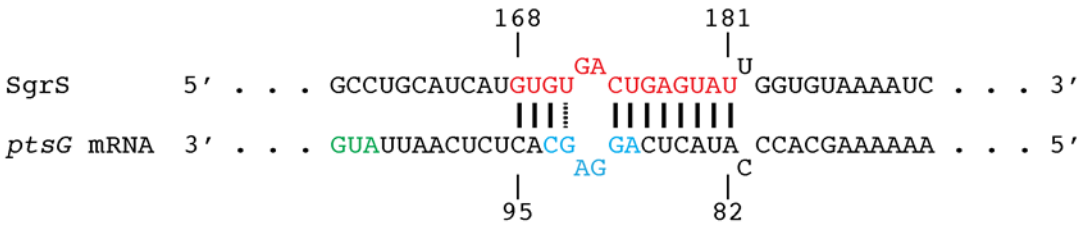

Green nucleotides form the Start Site
Blue nucleotides form the Ribosome Binding Site

Figure 1. Target search kinetics of SgrS. (a) Kinetic scheme of *ptsG* mRNA degradation induced by wild-type SgrS sRNA and the different SgrS point mutants. The figure shows one of the SgrS mutant strains, A177U. The steps are described in detail in the main text and the inset shows the mutants used in this study. [*p*], [*S*] and [*Sp*] are the concentrations of *ptsG* mRNA, SgrS and the SgrS-*ptsG* complex, respectively, in their mass-action equations. **(b)** Secondary structure of SgrS sRNA from nucleotide 168 to the poly-U tail. The nucleotide positions where mutations were made are boxed. The nucleotides involved in base-pairing with *ptsG* mRNA are red. **(c)** Base-pairing interaction between SgrS and *ptsG* mRNA showing the complementary region, start site and ribosome binding site.

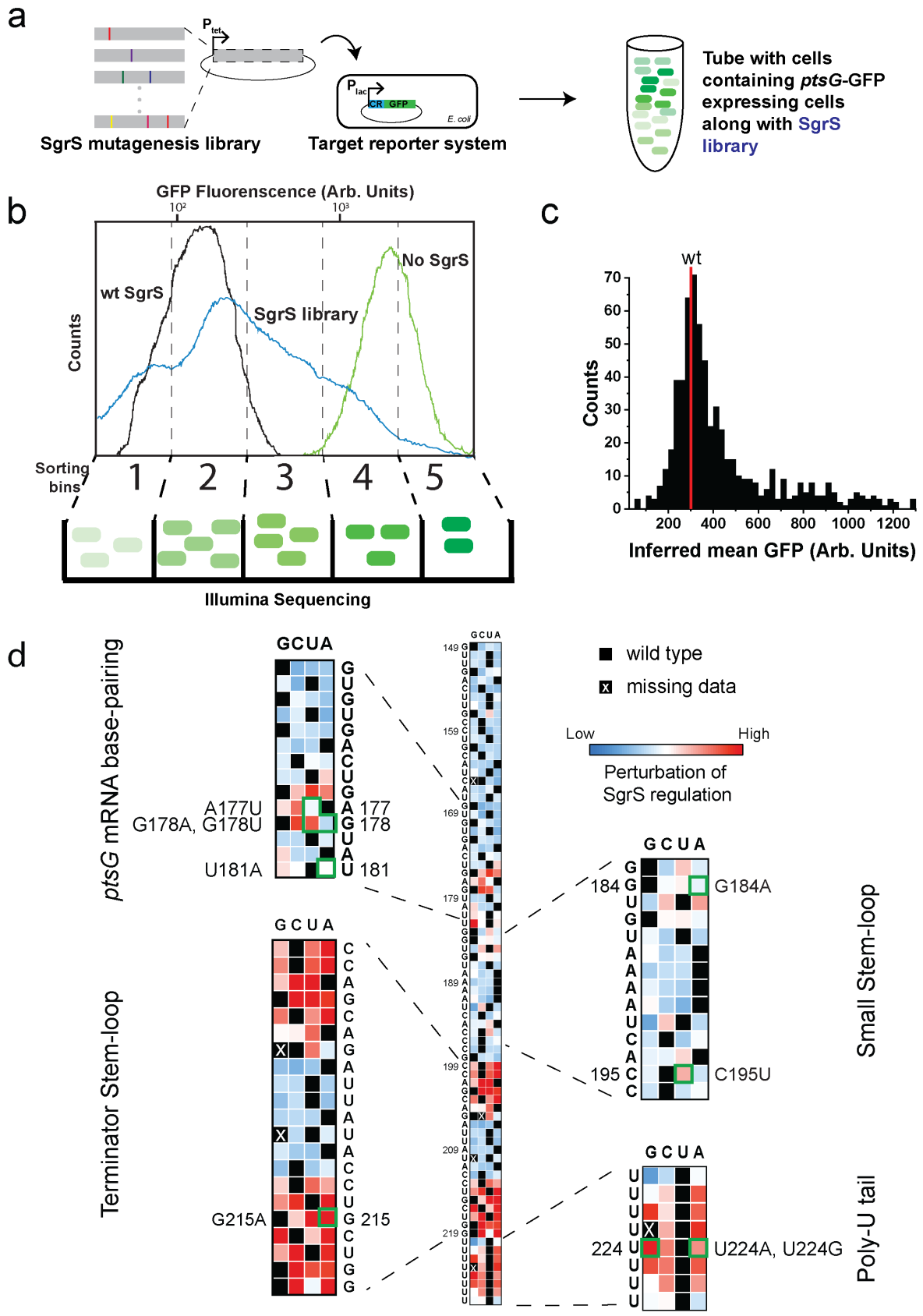
a
SgrS mutagenesis library
Target reporter system
Tube with cells containing ptsG-GFP expressing cells along with SgrS library
b
GFP Fluorescence (Arb. Units)
wt SgrS
SgrS library
No SgrS
Counts
Sorting bins
1
2
3
4
5
Illumina Sequencing
c
wt
Counts
Inferred mean GFP (Arb. Units)
d
ptsG mRNA base-pairing
Terminator Stem-loop
Small Stem-loop
Poly-U tail
A177U
G178A, G178U
U181A
G215A
G184A
C195U
U224A, U224G
wild type
missing data
Low
High
Perturbation of SgrS regulation

Figure 2. Mapping efficacy of SgrS regulation of *ptsG* mRNA with respect to its sequence. **(a)** Preparation of SgrS mutation library. Mutations were introduced into the SgrS plasmid using mutagenesis PCR. This library was then transformed into an *E. coli* strain already transformed with the *ptsG* mRNA plasmid fused with a GFP reporter. **(b)** Sorting of the cells and sequencing. The cells with two-plasmid co-expression were sorted using flow cytometry. The SgrS library (blue) shows GFP fluorescence that spans the region from the wild-type SgrS (black) to target (*ptsG*)-only (green). Cells were sorted into 5 evenly spaced (log scale) fluorescence bins and the occupancy percentages were 18.74%, 33.76%, 30.91%, 13.83% and 2.76% respectively. The cells from each bin were grown, DNA was purified, barcoded and sequenced using Illumina sequencing platform. **(c)** Histogram of the Sort-Seq measurements from the SgrS library from two replicates combined. The mean fluorescence for the wild-type SgrS is shown in red. **(d)** Heat map showing the effect of mutations on SgrS regulation of *ptsG* mRNA starting from nucleotide 149 to 227. The colors in the boxes are scaled from blue (low) to red (high), according to the level of perturbation of SgrS regulation. Black squares represent the wild-type base at each position and the black boxes with white crosses show the position of the mutants missing in the experiment. Text shows the wild type sequence of SgrS. Insets show the four regions of SgrS, viz. base-pairing region, small stem-loop, terminator stem-loop and the poly-U tail.

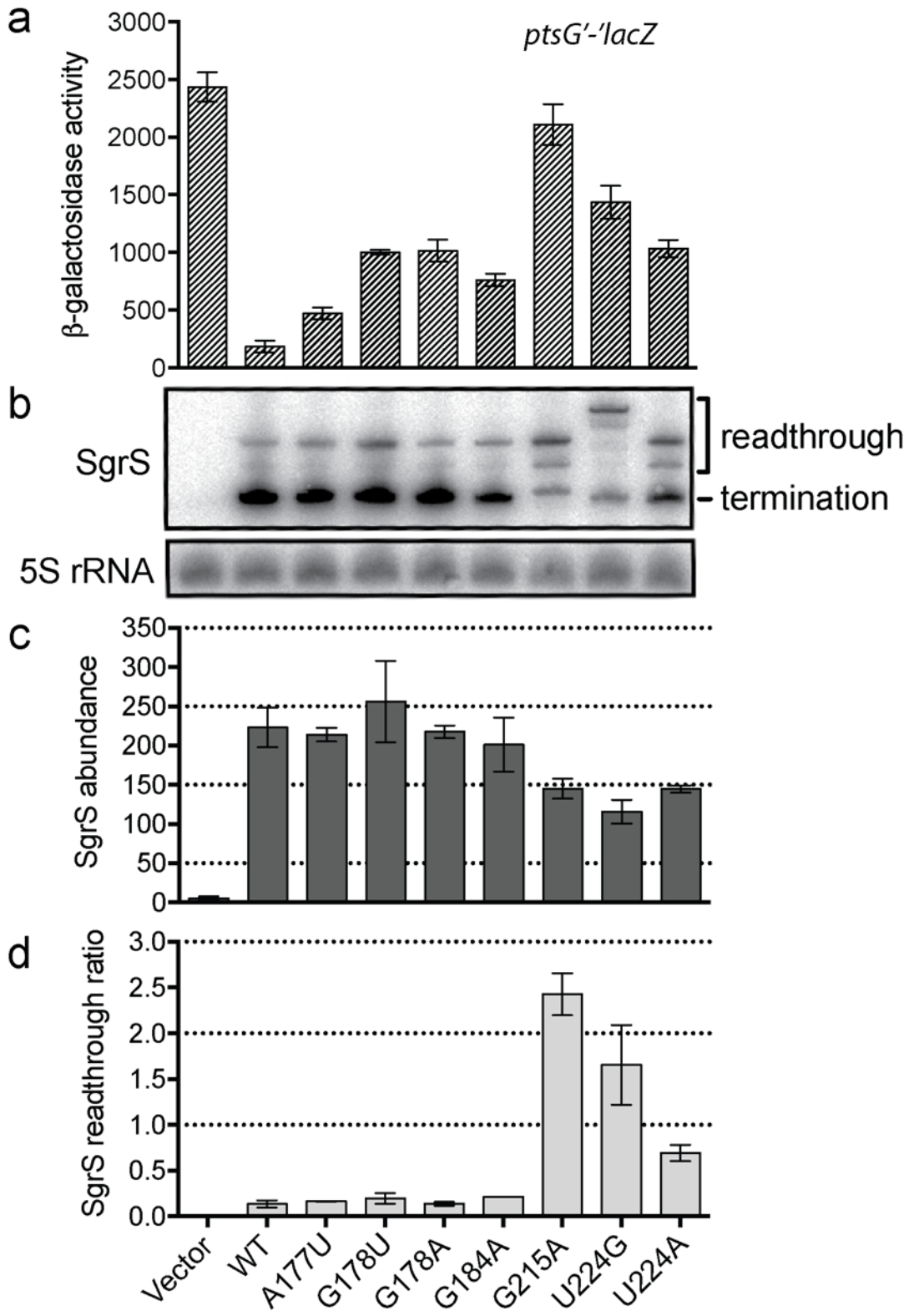
a
ptsG'-'lacZ
β-galactosidase activity
3000
2500
2000
1500
1000
500
0
b
SgrS
readthrough
termination
5S rRNA
c
SgrS abundance
350
300
250
200
150
100
50
0
d
SgrS readthrough ratio
3.0
2.5
2.0
1.5
1.0
0.5
0.0
Vector
WT
A177U
G178U
G178A
G184A
G215A
U224G
U224A

Figure 3. Regulation of *ptsG'-'lacZ* translational fusion by SgrS point-mutants. (a) Regulation of chromosomal *ptsG'-'lacZ* translational fusion by wild-type SgrS and A177U, G178U, G178A, G184A, G215A, U224A, U224G mutant variants (plasmid-encoded) was assessed using β-galactosidase activity assay. Standard error was calculated based on data from four biological replicates. **(b)** RNA was extracted simultaneously with β-galactosidase activity assay and Northern blot was performed using probes specific for SgrS sRNA and 5S rRNA (control). Full-length (227 nt), properly terminated SgrS transcripts are labeled as "termination" products, and longer transcripts that arose due to transcriptional readthrough are labeled as "readthrough" products. **(c)** Band intensities of total SgrS transcripts (termination+readthrough) were measured, and 5S-normalized values were plotted as "SgrS abundance" (steady state transcript abundance of SgrS mutants). **(d)** Band intensities of SgrS termination and readthrough products were measured and 5S-normalized ratios (readthrough/termination) were calculated and plotted for each SgrS mutant as "SgrS readthrough ratio".

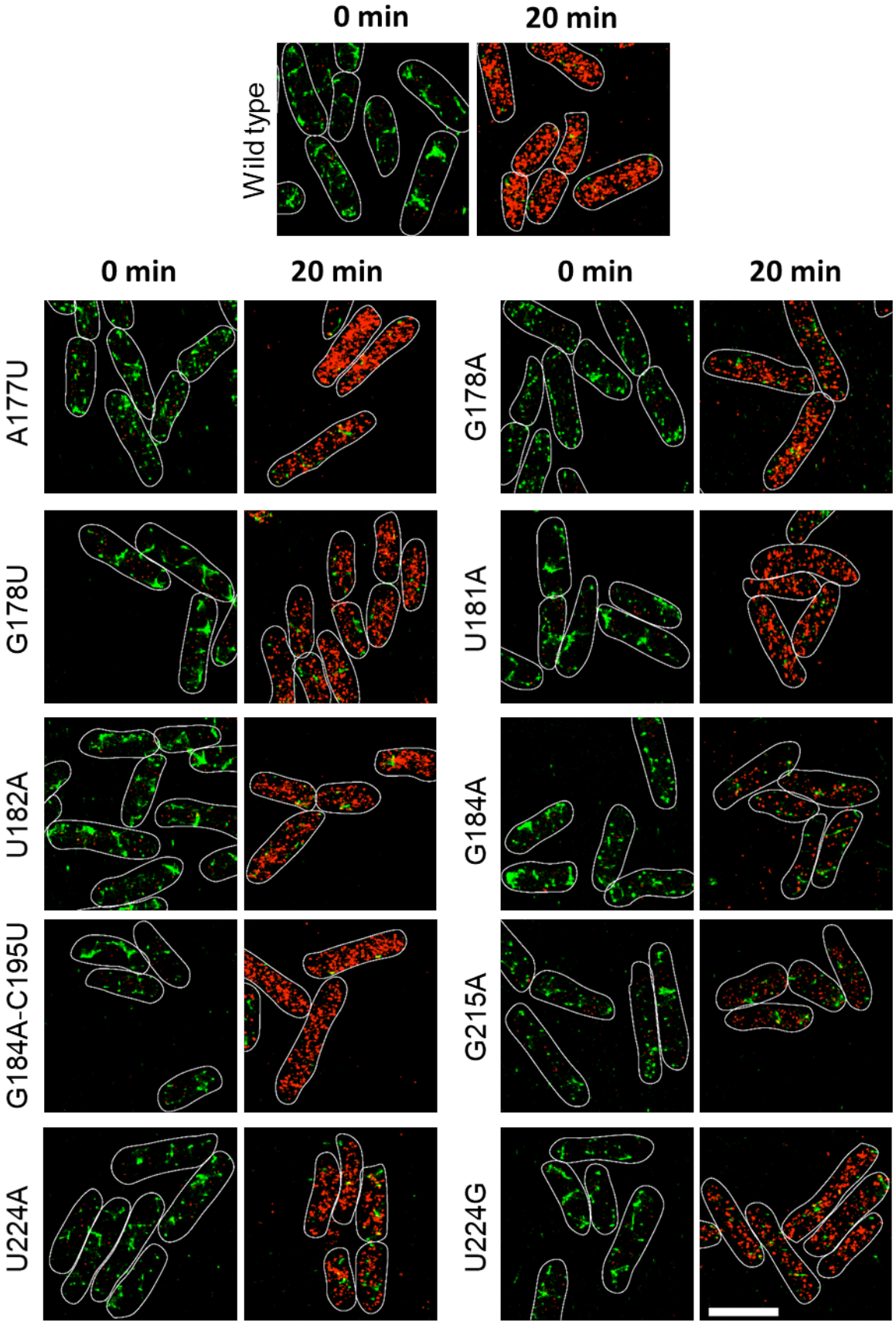

SgrS *ptsG* mRNA

Figure 4. 3D super-resolution images projected in 2D planes. The panels show SgrS (red) and *ptsG* mRNA (green) labeled by smFISH for the wild-type and the mutant strains, A177U, G178A, G178U, U181A, U182A, G184A, G184A-C195U, G215A, U224A, U224G before and after 20 minutes of αMG (non-metabolizable sugar analogue) induction. Cell boundaries are denoted by white solid lines. Scale bar is 2 μm.

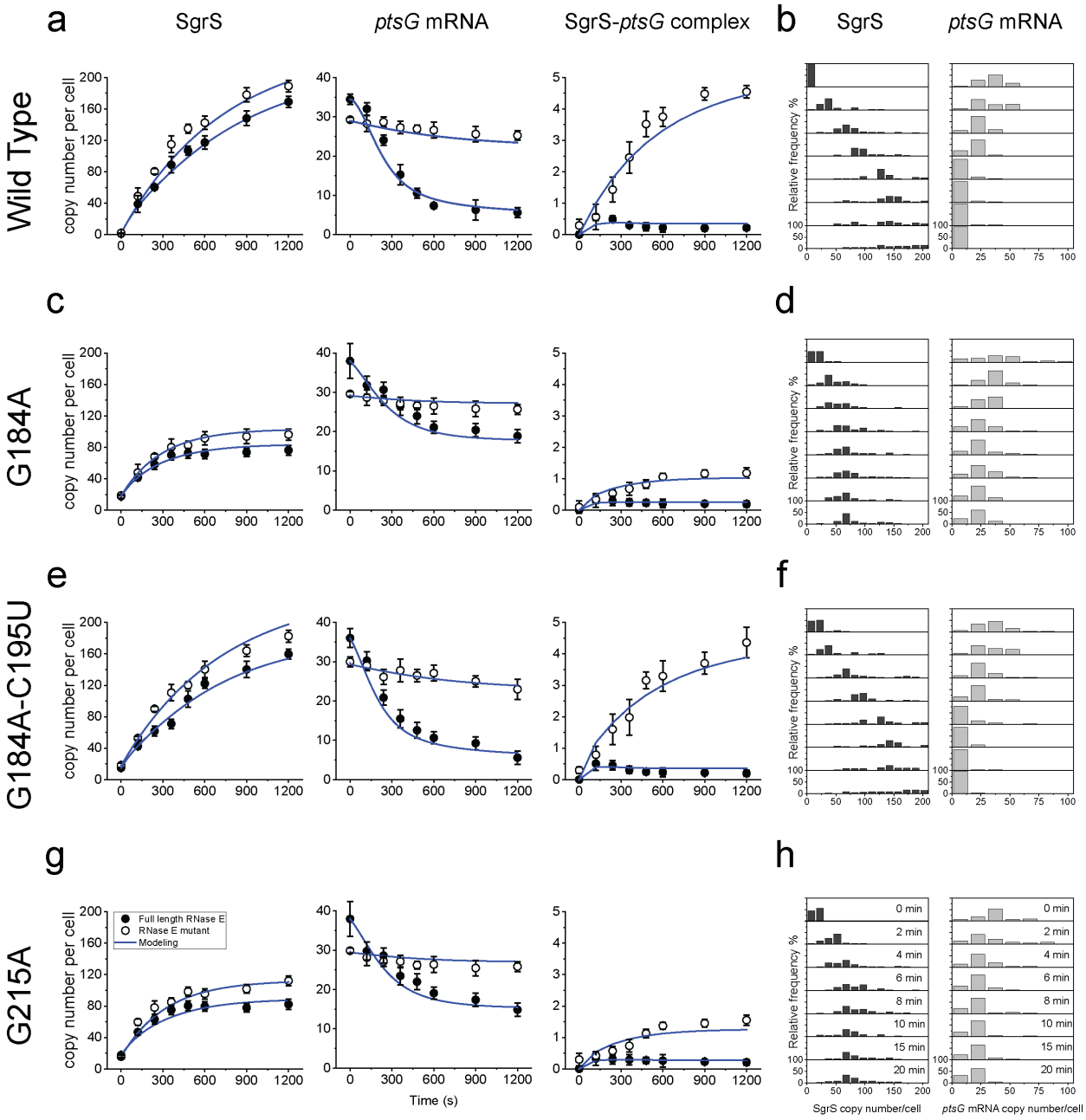

Figure 5. Time dependent changes in the copy numbers of SgrS and *ptsG* mRNA and estimation of kinetic parameters. Time course changes and corresponding modeling curves for the SgrS, *ptsG* mRNA and SgrS-*ptsG* complex in **(a)** wild-type, **(c)** G184A mutant strain, **(e)** G184A-C195U mutant strain, **(g)** G215A mutant strain. Average copy numbers per cell are plotted against time. Rate constants obtained for these mutants are shown in Figure 6 and in

Supplementary Table 3. Weighted R^2's for modeling are also reported in Supplementary Table 4. Error bars in **(a)**, **(c)**, **(e)**, **(g)** are standard errors from 80 to 150 cells in each case. Histograms showing the change in distribution of SgrS and *ptsG* mRNA copy numbers for **(b)** wild-type, **(d)** G184A mutant strain, **(f)** G184A-C195U mutant strain, **(h)** G215A mutant strain for 80-150 cells in each case.

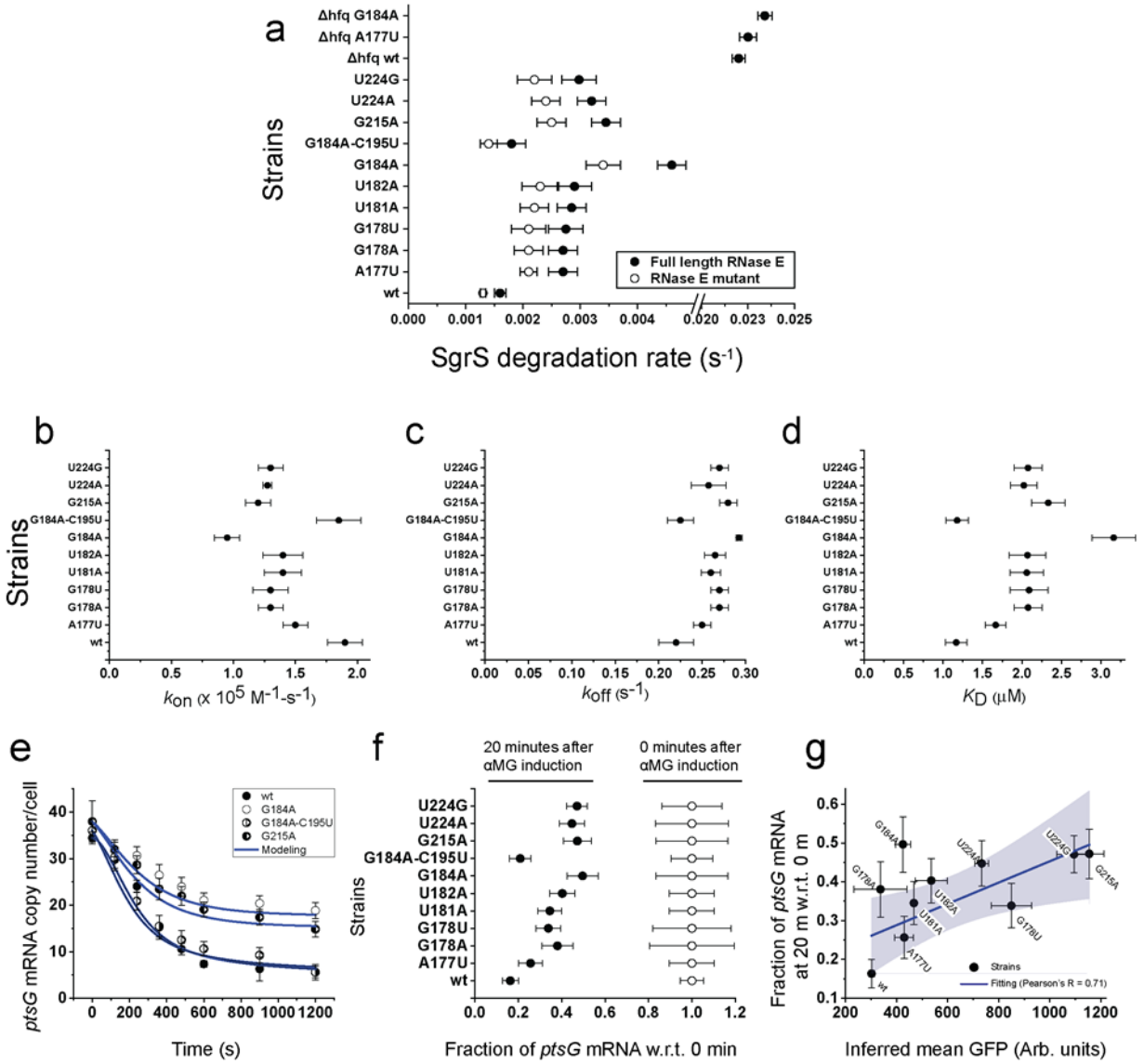

Figure 6. Calculation of various parameters and correlation with Sort-Seq. (a) Degradation rates of SgrS for the wild-type and the strains A177U, G178A, G178U, U181A, U182A, G184A, G184A-C195U, G215A, U224A, U224G, Δ*hfq* wild type, Δ*hfq* A177U, Δ*hfq* G184A for full length RNase E and RNase E mutants. Error bars represent standard deviation from two experimental replicates. **(b-d)** k_{on}, k_{off}, K_D measured from the time dependent modeling curves of the SgrS, *ptsG* mRNA and SgrS-*ptsG* mRNA complexes for the wild-type and strains A177U,

G178A, G178U, U181A, U182A, G184A, G184A-C195U, G215A, U224A, U224G. These were determined simultaneously in the wild-type and RNase E mutants. Error bars report standard deviation from the independent fitting on two replicates. **(e)** Time course changes in *ptsG* mRNA for the wild-type, G184A, G184A-C195U, G215A mutant strains. Error bars represent standard errors from 80-150 cells in each case. **(f)** Fractional change in *ptsG* mRNA copy numbers for the wild-type and the mutants A177U, G178A, G178U, U181A, U182A, G184A, G184A-C195U, G215A, U224A, U224G before and after 20 minutes αMG induction. Error bars represent standard errors from 80-150 cells in each case. **(g)** Comparison of the SgrS regulation efficacy calculated from Sort-Seq assay and the imaging-based analysis. Error bars in the x-axis are standard deviations calculated from two experimental replicates and those in the y-axis are as described in **(f)**. The fitting is shown in blue and the grey region shows the 95% confidence region.